Eur. Phys. J. A (2022) 58:117
https://doi.org/10.1140/epja/s10050-022-00758-y

THE EUROPEAN PHYSICAL JOURNAL A

Regular Article - Theoretical Physics

Study of spatial structures in α-cluster nuclei

V. V. Samarin[1,2,a]

[1] Flerov Laboratory of Nuclear Reactions, Joint Institute for Nuclear Research, 6 Joliot Curie Street, Dubna, Moscow Region 141980, Russia
[2] Department of Nuclear physics, Dubna State University, 19 Universitetskaya Street, Dubna, Moscow Region 141982, Russia

Received: 21 October 2020 / Accepted: 1 June 2022

Communicated by D. Blaschke

Abstract Calculations of the probability densities and energies of the ground states for α-cluster nuclei ^{12}C (3α), ^{16}O (4α), ^{20}Ne (5α), ^{24}Mg (6α), ^{28}Si (7α) and for nuclear molecules ^{9}Be ($2\alpha+n$), ^{10}Be ($2\alpha+2n$), ^{10}B ($2\alpha+n+p$), ^{10}C ($2\alpha+2p$), ^{11}B ($2\alpha+2n+p$), ^{11}C ($2\alpha+n+2p$) were performed by the Feynman Path Integral method using parallel computing based on NVIDIA CUDA technology. In addition, ^{12}C (3α) was considered in three-body hyperspherical harmonics formalism with a new effective method of solving hyperradial equation using cubic spline interpolation. The spatial structures of the ground states of ^{12}C and ^{16}O correspond to simple geometric shapes, a regular triangle and a tetrahedron, respectively, with wide α-cluster clouds in their vertices. The ^{24}Mg nucleus has the shape of a pair of equal regular triangles with wide α-cluster clouds in their vertices as well. The nuclei ^{9}Be, ^{10}Be, ^{10}B, ^{10}C, ^{11}B, ^{11}C have molecular structure with valence neutrons and/or protons between two α-clusters.

1 Introduction

It is well known, that ^{12}C, ^{16}O, ^{20}Ne, ^{24}Mg, and ^{28}Si nuclei may be represented as composed of N α-particles (α-clusters) with $N = 3, 4, 5, 6, 7$, respectively [1,2]. In particular, the energy E_s of separation of the ^{12}C nucleus into three α-particles is equal to $E_s = 7.27$ MeV and it is substantially smaller than the energies of separation of a proton $E_{s,p} = 15.96$ MeV or a neutron $E_{s,p} = 18.72$ MeV (see, e.g., [3]). The ^{9}Be and ^{10}Be nuclei may be represented as composed of two α-particles (α-clusters) and respectively one and two outer (valence) weakly bound neutrons [4–10]. They may be regarded as simple two-center nuclear molecules [11–13]. The α-cluster model explains the large deformation of the ^{9}Be and ^{10}Be nuclei (for ^{9}Be the quadrupole deformation parameter is $\beta_2 = 0.89$ [14]). The α-cluster structure of the ^{9}Be nucleus is manifested in scattering, breakup, and fusion [15] as well as in the nucleon and cluster transfer reactions [16]. An addition of two protons to the ^{10}Be nucleus significantly changes its structure (into the ^{12}C (3α) nucleus). Clustering in nuclei leads to some specific spatial structures which can affect various observables associated with these nuclei. The examples of these structures are dineutron and cigar configurations in ^{6}He [17–21] as well configurations $\alpha+d$ and $\alpha+t$ in the ^{6}Li and ^{7}Li nuclei accordingly [22–26]. In this work, the spatial structures in $N\alpha$-cluster nuclei ^{12}C, ^{16}O, ^{24}Mg and cluster nuclei with few nucleons ^{9,10}Be, ^{10,11}B, ^{10,11}C (nuclear molecules) are studied.

There are two general approaches to studying stationary states in quantum mechanics. The first, and the main one, is based on the Schrödinger equation. The second is based on the Feynman Path Integral (FPI) method [27]. There are many methods for an approximate solution of the multi-dimensional stationary Schrödinger equation. The three-body problem was solved using the hyperspherical functions (HSF) method [15,18–20,28–30], Gaussian basis and numeric solution of the Hill–Wheeler integral equations [24,31], variational Gaussian-expansion method [29,30,32], stochastic variational method [33], Lagrange mesh methods [29,30,34,35], continuum-discretized coupled-channel approach and finite elements method [36,37], Faddeev equations [38,39], Faddeev–Yakubovsky equations [40], generator coordinate method [41], Tohsaki–Horiuchi–Schuck-Röpke (THSR) wave function [4,5,8–10,41–43] and some others. The $N\alpha$ systems were studied using the hyperspherical harmonics basis [44]. Application of hyperspherical expansion for heavier nuclei is limited by the large size of the model space and the large numbers of matrix elements in the hyperspherical basis [44].

The FPI method is used because it is not limited by the number of the particles. The reason why FPI is a natural choice for studying spatial structures is because the asymptotic form of the FPI kernel contains density distributions

[a] e-mail: samarin@jinr.ru (corresponding author)

Published online: 04 July 2022

explicitly. To demonstrate the capabilities of this method, we first compare it with the HSF method for the systems of three particles. In Sect. 2, the FPI method is described and tested for the ground states of two exactly solvable oscillatory systems. In Sect. 3, the hyperspherical formalism for zero orbital angular momentum together with a new method for solution of the hyperradial equations with the cubic splines interpolation are described. In Sect. 4, α–α potentials $V_{\alpha-\alpha}$ are discussed and the results for $N\alpha$ systems with $2 \leq N \leq 7$ are presented. The connection between the separation energies E_s, the potential $V_{\alpha-\alpha}$, and the spatial structures in the ground states of the nuclei ^{12}C, ^{16}O, ^{24}Mg is studied. In Sect. 5, nucleon-nucleon and α-nucleon potentials are discussed and the results obtained for the nuclei ^{3}H, ^{3}He, ^{9,10}Be, ^{10,11}B, ^{10,11}C are presented.

2 Feynman path integral method

Feynman path integral is a propagator-the probability amplitude for a particle to travel from a point $\mathbf{q}_0$ in an s-dimensional space to a point $\mathbf{q}$ in a given time t [27]:

$$K\left(\mathbf{q}, t; \mathbf{q}_0, 0\right) = \int D\mathbf{q}(t') \exp\left\{\frac{i}{\hbar} S\left[\mathbf{q}(t')\right]\right\} = \langle \mathbf{q}| \exp\left(-\frac{i}{\hbar}\hat{H}t\right)|\mathbf{q}_0\rangle. \tag{1}$$

Here, $S[\mathbf{q}(t)]$ and $\hat{H}$ are the action and the Hamiltonian of the system, respectively, and $D\mathbf{q}(t)$ is the integration measure [45]. For a time-independent potential energy $V(\mathbf{q})$, transition to the imaginary time $t = -i\tau$ yields the propagator $K_{\mathrm{E}}(\mathbf{q}, \tau; \mathbf{q}_0, 0)$:

$$K_{\mathrm{E}}\left(\mathbf{q}, \tau; \mathbf{q}_0, 0\right) = \int D_E\mathbf{q}(\tau) \exp\left\{-\frac{1}{\hbar} S_E\left[\mathbf{q}(\tau')\right]\right\} \tag{2}$$

with the Euclidean action

$$S_{\mathrm{E}}\left[\mathbf{q}(\tau')\right] = \int_0^\tau d\tau' \left[\frac{m}{2}\left(\frac{d\mathbf{q}}{d\tau'}\right)^2 + V(\mathbf{q})\right]. \tag{3}$$

The propagator $K_{\mathrm{E}}(\mathbf{q}, \tau; \mathbf{q}, 0)$ has the following asymptotic behavior [46]:

$$K_{\mathrm{E}}(\mathbf{q}, \tau; \mathbf{q}, 0) \to |\psi_0(\mathbf{q})|^2 \exp\left(-\frac{E_0\tau}{\hbar}\right) + |\psi_1(\mathbf{q})|^2 \exp\left(-\frac{E_1\tau}{\hbar}\right) + \ldots, \ \tau \to \infty, \tag{4}$$

where E_0 and E_1 are the energies of the ground and the first excited states with the wave functions $\psi_0(\mathbf{q})$, $\psi_1(\mathbf{q})$. For the bound states of the N-body system, the energies are negative. The expression

$$\hbar \ln K_{\mathrm{E}}(\mathbf{q}, \tau; \mathbf{q}, 0) \to \hbar \ln |\Psi_0(\mathbf{q})|^2 - E_0\tau, \ \tau \to \infty \tag{5}$$

was used to obtain the energy E_0 as the slope of the linear part of the graph representing $\ln K_E(\mathbf{q}, \tau; \mathbf{q}, 0)$ as a function of τ. The squared modulus of the ground state wave function $|\Psi_0(\mathbf{q})|^2$ in the points q of the finite region corresponding to finite motion can be determined based on expression (4) at τ values in the linear part of the graph of dependence $\ln K_E(\mathbf{q}, \tau; \mathbf{q}, 0)$ near its inflection point.

Feynman path integral for a one-dimensional system may be represented as the limit of a multiple integral [46,47]:

$$K_{\mathrm{E}}(q, \tau; q_0, 0) = \lim_{N\to\infty} \int \cdots \int \exp\left\{-\frac{1}{\hbar}\sum_{k=1}^{N}\left[\frac{m(q_k - q_{k-1})^2}{2\Delta\tau} + V(q_k)\Delta\tau\right]\right\} \times C^N dq_1 dq_2 \ldots dq_{N-1}, \tag{6}$$

where $q_k = q(\tau_k)$, $\tau_k = k\Delta\tau$, $k = \overline{0, N}$, $N\Delta\tau = \tau$,

$$C = \left(\frac{m}{2\pi\hbar\Delta\tau}\right)^{1/2}. \tag{7}$$

In order to calculate approximately the path integral in Eq. (6), one singles out the Euclidean propagator $K_{\mathrm{E}}^{(0)}$ of a free-particle:

$$K_{\mathrm{E}}(q, \tau; q_0, 0) \approx K_{\mathrm{E}}^{(0)}(q, \tau; q_0, 0) \times \left\langle \exp\left[-\frac{\Delta\tau}{\hbar}\sum_{k=1}^{N} V(q_k)\right]\right\rangle_{0,N}, \tag{8}$$

$$K_{\mathrm{E}}^{(0)}(q, \tau; q_0, 0) = \left(\frac{m}{2\pi\hbar\tau}\right)^{1/2} \exp\left[-\frac{m(q - q_0)^2}{2\hbar\tau}\right]. \tag{9}$$

Setting $q_N = q_0 = q$, we obtain

$$K_{\mathrm{E}}(q, \tau; q, 0) \approx \left(\frac{m}{2\pi\hbar\tau}\right)^{1/2} \left\langle \exp\left[-\frac{\Delta\tau}{\hbar}\sum_{k=1}^{N} V(q_k)\right]\right\rangle_{0,N}. \tag{10}$$

Here and below, angular brackets denote averaging of the quantity f

$$f = \exp\left[-\frac{\Delta\tau}{\hbar}\sum_{k=1}^{N} V(q_k)\right] \tag{11}$$

over arbitrary trajectories-$(N-1)$-dimensional vectors $Q = \{q_1, \ldots, q_{N-1}\}$ with the multidimensional Gaussian distribution [48]:

$$W(q_0; q_1, \ldots, q_{N-1}; q_N = q_0) = C^{N-1} N^{1/2} \exp\left[-\frac{m}{2\hbar\Delta\tau}\sum_{k=1}^{N}(q_k - q_{k-1})^2\right]. \tag{12}$$

Averaging of the quantity f can be performed by the Monte–Carlo method:

$$\langle f\rangle \approx \frac{1}{n}\sum_{i=1}^{n} f_i. \tag{13}$$

A standard algorithm for simulating a random vector satisfying the distribution law in (12) is presented in Appendix. Because of random errors in simulation, a linear regression should be used in expression (5) to determine the ground state energy.

For s-dimensional vectors $\mathbf{q}$, the propagator $K_{\mathrm{E}}(\mathbf{q}, \tau; \mathbf{q}_0, 0)$ is calculated as

$$K_{\mathrm{E}}(\mathbf{q}, \tau; \mathbf{q}, 0) \approx \left(\frac{m}{2\pi\hbar\tau}\right)^{s/2} \left\langle \exp\left[-\frac{\Delta\tau}{\hbar}\sum_{k=1}^{N} V(\mathbf{q}_k)\right]\right\rangle. \tag{14}$$

The values of the propagator were calculated based on Jacobi coordinates, the Monte–Carlo method, and averaging over $n \gg 1$ random trajectories $\mathbf{q}_k, k = \overline{0, N}, \mathbf{q}_0 = \mathbf{q}_N$, $N \gg 1$. Parallel calculations of the K_{E} values [49] using NVIDIA CUDA technology [50,51] were performed mainly on the Heterogeneous Cluster of the Joint Institute for Nuclear Research [52]. Parallel calculations reduce computing time when solving N-body problems using the FPI method by three orders of magnitude [49]; this makes it possible to perform them on ordinary laptops.

For verifying and testing the FPI method in the system of units with $\hbar = 1$, we used two harmonic oscillatory systems in which particles interact with each other by the pairwise potential:

$$V(r) = \frac{1}{2}r^2 \tag{15}$$

and the total potential energy had a constant shift U_0:

$$V = -U_0 + \sum_{i<j}\frac{1}{2}r_{ij}^2. \tag{16}$$

The first system (I) consisted of three particles with masses $m_1 = m_2 = 1, m_3 = \infty$, the normal mode frequencies are equal to

$$\Omega_1 = \sqrt{3},\ \Omega_2 = 1. \tag{17}$$

and the ground state energy for $U_0 = 0$ is

$$E_0 = \frac{3}{2}\left(1 + \sqrt{3}\right) = 4.098. \tag{18}$$

The second system (II) consisted of N particles with equal masses $m = 1$ and the ground state energy is

$$E_0 = -U_0 + \frac{3}{2}(N-1)\sqrt{N}. \tag{19}$$

The results of the FPI calculations of $\ln K_{\mathrm{E}}$ as a function of τ for grid spacing in imaginary time $\Delta\tau = 0.01$ are shown in Fig. 1. The ground state energy calculated as the slope of the linear part of the graph of $\ln K_{\mathrm{E}}$ is given in Table 1. One can see that the FPI method yields the exact values of the ground state energy with small uncertainties, which makes it possible to use this method in calculations of the ground state

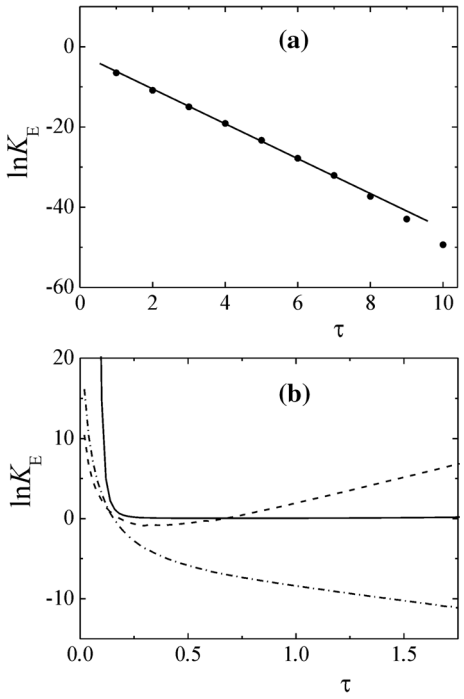

Fig. 1 Dependence of $\ln K_{\mathrm{E}}$ (14) on imaginary time τ for N-body systems with oscillatory potential energy (16) (I) with $U_0 = 0$ (**a**) and (II) with $U_0 = -20$ (**b**) in the system of units with $\hbar = 1$. (**a**) Dots are the result of calculations and the straight line is the result of the linear regression applied to the linear interval of the graph. (**b**) Results for $N = 5$ (dash-dotted curve), $N = 6$ (solid curve), and $N = 7$ (dashed curve)

energies for nuclear N-body systems with $N > 3$. The aim of this paper is to study spatial distributions which will not be much affected by the FPI uncertainties for 3-body systems.

Below, the dimensionless variables are used

$$\tilde{K}_{\mathrm{E}}(\tilde{\mathbf{q}}, \tilde{\tau}; \tilde{\mathbf{q}}, 0) \approx \left(\frac{\tilde{m}}{2\pi\tilde{\tau}}\right)^{s/2} \left\langle \exp\left[-\Delta\tilde{\tau} b_0 \sum_{k=1}^{N}\tilde{V}(\tilde{\mathbf{q}}_k)\right]\right\rangle_{0,N}, \tag{20}$$

where $\tilde{K}_{\mathrm{E}} = K_{\mathrm{E}} x_0^s$, $\tilde{\mathbf{q}} = \mathbf{q}/x_0$, $x_0 = 1$ fm, $\tilde{m} = m/m_0$, m_0 is the neutron mass, $\tilde{V} = V/\varepsilon_0$, $\varepsilon_0 = 1$ MeV, $\tilde{\tau} = \tau/t_0$, $\tau = N\Delta\tau$, $\Delta\tilde{\tau} = \Delta\tau/t_0$,

$$t_0 = m_0 x_0^2/\hbar \approx 1.588 \cdot 10^{-23} s, \tag{21}$$

$$b_0 = t_0\varepsilon_0/\hbar \approx 0.0241. \tag{22}$$

The equation

$$b_0{}^{-1} \ln \tilde{K}_{\mathrm{E}}(\tilde{\mathbf{q}}, \tilde{\tau}; \tilde{\mathbf{q}}, 0) \approx b_0{}^{-1} \ln|\psi_0(\tilde{\mathbf{q}})|^2 - \tilde{E}_0\tilde{\tau} \tag{23}$$

is used to obtain the dimensionless energy $\tilde{E}_0 = E_0/\varepsilon_0$ as the slope of the linear part of the graph of $\ln \tilde{K}_{\mathrm{E}}$ as a function of $\tilde{\tau}$.

Table 1 The exact $E_{0,\mathrm{ex}}$ and calculated (using HSF and FPI methods) $E_{0,\mathrm{calc}}$ values of the ground state energies of N-body oscillatory systems (I) and (II) with potential energy (12) in the system of units with $\hbar = 1$

System, U_0	N	$E_{0,\mathrm{ex}}$	$E_{0,\mathrm{calc}}$	Method, parameter ($\Delta\rho$ for HSF; n for FPI)
I, 0	3	4.098	4.139 ± 0.12	HSF, 0.4
I, 0	3	4.098	4.11 ± 0.12	HSF, 0.2
I, 0	3	4.098	4.10 ± 0.12	HSF, 0.1
I, 0	3	4.098	4.11 ± 0.01	FPI, 10^5
II, −20	5	−6.584	-6.578 ± 0.005	FPI, 10^7
II, −20	6	−1.629	-1.84 ± 0.01	FPI, 10^7
II, −20	7	3.812	3.71 ± 0.02	FPI, 10^5

Before applying the FPI method to 4- and 5-body systems we will test it for a 3-body system ^{12}C, for which we will also use another method, the hyperspherical harmonics method, described in the next section.

3 Hyperspherical functions method

In the HSF method for nuclear 3-body systems, we use the *normalized* dimensionless variables (Jacobi coordinates):

$$\tilde{\mathbf{x}}_i = \sqrt{\frac{\tilde{m}_j \tilde{m}_k}{\tilde{m}_j + \tilde{m}_k}}(\tilde{\mathbf{r}}_j - \tilde{\mathbf{r}}_k), \tag{24}$$

$$\tilde{\mathbf{y}}_i = \sqrt{\frac{\tilde{m}_i(\tilde{m}_j + \tilde{m}_k)}{\tilde{m}_1 + \tilde{m}_2 + \tilde{m}_3}}\left(-\tilde{\mathbf{r}}_i + \frac{\tilde{m}_j \tilde{\mathbf{r}}_j + \tilde{m}_k \tilde{\mathbf{r}}_k}{\tilde{m}_j + \tilde{m}_k}\right), \tag{25}$$

where $\tilde{\mathbf{r}} = \mathbf{r}/x_0$ and $\tilde{m} = m/m_0$ are dimensionless radius vectors and masses of particles, respectively, $x_0 = 1$ fm, m_0 is the neutron mass, the same as in FPI calculations. The hyperspherical coordinates are $\Omega = \{\theta_x, \varphi_x, \theta_y, \varphi_y, \alpha\}, \tilde{x} = \rho\cos\alpha$, $\tilde{y} = \rho\sin\alpha$; ρ is the dimensionless hyperradius

$$\rho^2 = \tilde{\mathbf{x}}_1^2 + \tilde{\mathbf{y}}_1^2 = \tilde{\mathbf{x}}_2^2 + \tilde{\mathbf{y}}_2^2 = \tilde{\mathbf{x}}_3^2 + \tilde{\mathbf{y}}_3^2. \tag{26}$$

The hyperspherical harmonics (functions) are

$$\Phi_{KLM}^{l_x l_y}(\Omega) = \sum_{m_x m_y} (l_x l_y m_x m_y | LM) \Phi_{KL}^{l_x l_y m_x m_y}(\Omega), \tag{27}$$

$$\Phi_{KL}^{l_x l_y m_x m_y}(\Omega) = g_K^{l_x l_y}(\alpha) Y_{l_x m_x}(\hat{x}) Y_{l_y m_y}(\hat{y}); \tag{28}$$

$(l_x l_y m_x m_y | LM)$ are the Clebsch-Gordon coefficients; $Y_{l_x m_x}(\hat{x})$, $Y_{l_y m_y}(\hat{y})$ are spherical harmonics; l_x is the angular momentum of a pair of particles of the system. The orbital angular momentum for the ground state is equal to zero, $L = 0$; therefore, $l_y = l_x$ and

$$g_{K0}^{l_x l_x}(\alpha) = N_K^{l_x l_x} (\cos\alpha)^{l_x} (\sin\alpha)^{l_x} P_n^{l_x+1/2, l_x+1/2}(\cos 2\alpha); \tag{29}$$

$P_n^{l_x+1/2, l_x+1/2}(t)$ are the Jacobi polynomials; $K = 2n + 2l_{x_i}$ is the hypermoment; $n = 0, 1, 2\ldots, l_x = 0, 2, \ldots$. Expansion of the wave function Ψ_0 into hyperspherical functions for $L = 0$ is

$$\Psi_0(x, y, \cos\theta) = \tilde{\Psi}_0(\alpha, \theta, \rho) = \sum_{l_x K} \varphi_K^{l_x}(\rho) \rho^{-5/2} \Phi_{K00}^{l_x l_x}(\Omega)$$
$$= \sum_{l_x K} f_{K0}^{l_x l_x}(\rho) g_{K0}^{l_x l_x}(\alpha) (2l_x + 1) P_{l_x}(\cos\theta), \tag{30}$$

$$\varphi_K^{l_x}(\rho) = \rho^{5/2} f_{K0}^{l_x l_x}(\rho) (2l_x + 1), \varphi_K^{l_x}(0) = 0, \tag{31}$$

where θ is the angle between the Jacobi vectors. We take into account a set of N_s pairs of numbers (K, l_x) or (n, l_x) with the maximum hypermoment $K_{\max}$.

The system of N_s hyperradial equations for $L = 0$ is

$$\frac{d^2}{d\rho^2}\varphi_K^{l_x}(\rho) + \left[2\tilde{E}b_0 - \rho^{-2}(K + 3/2)(K + 5/2)\right]\varphi_K^{l_x}(\rho)$$
$$= 2b_0 \sum_{K' l_x'} \tilde{U}_{KK'}^{l_x; l_x'}(\rho) \varphi_{K'}^{l_x'}(\rho). \tag{32}$$

It contains the dimensionless coupling matrix $(N_s \times N_s)$:

$$\tilde{U}_{KK'}^{l_x; l_x'}(\rho) = \langle l_x l_x K 0 | \tilde{U} | l_x' l_x' K' 0 \rangle. \tag{33}$$

The calculations of the double integrals over angles α, θ in (33) were performed by the Gauss quadrature formula. The dimensionless potential energy of the system is represented as a sum of the pairwise potentials $\tilde{U} = (V_{12} + V_{13} + V_{23})/\varepsilon_0$. The functions $\varphi_K^{l_x}(\rho)$ have asymptotic behavior

$$\varphi_K^{l_x}(\rho) \sim \rho^\gamma, \rho \to 0, \tag{34}$$

where

$$\gamma = \frac{1}{2} + \sqrt{\frac{1}{4} + \left(K + \frac{3}{2}\right)\left(K + \frac{5}{2}\right)} \geq \frac{5}{2} \tag{35}$$

and conditions $\varphi_K^{l_x}(0) = 0$, $\varphi_K^{l_x\,\prime\prime}(0) = 0$ are satisfied.

There are several laborious methods for solving hyperradial equations, e.g., using the Sturmian basis [20,44], the basis of the Lagrange functions [15,28], and the Laguerre polynomial expansion [30]. A new method for solving hyperradial equations using cubic splines interpolation [53] was

proposed in [54]. The idea of this method is the simultaneous calculation of the mesh function φ_i and its second derivative η_i. As an example we show application of this method to hyperradial equations for $L = 0$.

The cubic spline interpolation expression [53] for the function $\varphi(\rho)$ may be written using its values $\varphi_0 = 0$, φ_i, $i = 1, ..., n_p$ and the values of its second derivative $\eta_i = \varphi''(\rho_i)$ in the mesh points ρ_i, $i = 0, 1, \ldots, n_p$, $\rho_{n_p} = \rho_{\max}$:

$$\varphi(\rho) = \eta_{i-1}\frac{(\rho_i-\rho)^3}{6h_i} + \eta_i\frac{(\rho-\rho_{i-1})^3}{6h_i} + \left(\varphi_{i-1} - \frac{\eta_{i-1}h_i^2}{6}\right)\frac{\rho_i-\rho}{h_i} + \left(\varphi_i - \frac{\eta_i h_i^2}{6}\right)\frac{\rho-\rho_{i-1}}{h_i}, \quad \rho \in [\rho_{i-1}, \rho_i], h_i = \rho_i - \rho_{i-1},\ i = 1, 2, \ldots, n_p. \tag{36}$$

With the additional natural boundary conditions $\eta_0 = \eta_{n_p} = 0$, the values of η_i are equal to

$$\eta = A^{-1}H\varphi, \varphi = \{\varphi_i\}, i = 1, ..., n_p - 1. \tag{37}$$

The square tridiagonal matrix A $[(n_p - 1) \times (n_p - 1)]$ has elements [53]:

$$A_{i\,i} = \frac{h_i + h_{i+1}}{3},\ A_{i\,i+1} = A_{i+1\,i} = \frac{h_{i+1}}{6},\ i = 1, \ldots, n_p - 1. \tag{38}$$

The square tridiagonal matrix H $[(n_p - 1) \times (n_p - 1)]$ has elements [53]:

$$H_{i\,i} = -h_i^{-1} - h_{i+1}^{-1},\ H_{i\,i+1} = H_{i+1\,i} = h_{i+1}^{-1},\ i = 1, \ldots, n_p - 1. \tag{39}$$

For the set of N_s hyperradial equations, we use the block matrices $\mathbf{A}$, $\mathbf{H}$ with the identity matrix I $(N_s \times N_s)$

$$\mathbf{A}_{i\,i} = I\frac{h_i + h_{i+1}}{3},\ \mathbf{A}_{i\,i+1} = \mathbf{A}_{i+1\,i} = I\frac{h_{i+1}}{6}, \tag{40}$$

$$\mathbf{H}_{i+1\,i} = Ih_{i+1}^{-1},\ \mathbf{H}_{i\,i} = -I(h_i^{-1} + h_{i+1}^{-1}),\ \mathbf{H}_{i\,i+1} = Ih_{i+1}^{-1},\ i = 1, \ldots, n_p - 1, \tag{41}$$

the diagonal block matrix

$$\mathbf{W}_{i\,i} = 2b_0\tilde{U}_{KK'}^{l_x;l'_x}(\rho_i) + \frac{1}{\rho_i^2}(K + 3/2)(K + 5/2)\delta_{KK'}\delta_{l_x;l'_x}, \tag{42}$$

and the block column matrix

$$\mathbf{F}_i = \{\varphi_K^{l_x}(\rho_i)\},\ i = 1, \ldots, n_p - 1. \tag{43}$$

The hyperradial equations on the mesh are

$$-\mathbf{A}^{-1}\mathbf{HF} + \mathbf{WF} = 2b_0E\mathbf{F}. \tag{44}$$

With the additional boundary conditions $\mathbf{F}_{n_p} = 0$, system (44) is the eigenvalue problem $\mathbf{BF} = \lambda\mathbf{F}$ for the square matrix $\mathbf{B}$ $[(n_p - 1)N_s \times (n_p - 1)N_s]$:

$$\mathbf{B} = -\mathbf{A}^{-1}\mathbf{HF} + \mathbf{WF} = 2b_0E\mathbf{F}. \tag{45}$$

For the equidistant mesh $h_i = \Delta\rho$, the matrix $\mathbf{B}$ is symmetric, eigenvalues λ are real and the eigenvectors $\mathbf{F}$ are orthogonal. Energies are equal to $E = \lambda/(2b_0)$. Smooth interpolation of the functions $\varphi_K^{l_x}(\rho)$ provides the possibility of decreasing the size of the hyperradial mesh n_p and the possibility of increasing the number of hyperradial equations N_s and the maximum hypermoment $K_{\max}$ in calculations for the systems with pairwise interactions having a repulsive core.

For verification testing of splines interpolation for solution of hyperradial equations, we used the harmonic oscillatory system (I) (15)–(18). The calculated ground state energy for $n = 0, 2; l_x = 0, 2; K_{\max} = 8; N_s = 6; \rho_{\max} = n_p\Delta\rho = 20$ is given in Table 1. One can see that splines interpolation in the HSF method provides the exact value with fast convergence when the value of $\Delta\rho$ decreases.

For the radial Schrödinger equation

$$-\psi'' + \frac{2m}{\hbar^2}U_{\text{eff}}(r)\psi(r) = \frac{2m}{\hbar^2}E\psi(r),\ 0 \le r \le r_{\max} \tag{46}$$

with the boundary conditions $\psi(0) = 0$, $\psi(r_{\max}) = 0$, splines interpolation leads to the eigenvalue problem:

$$B\psi = \lambda\psi,\quad B = -A^{-1}H + \tfrac{2m}{\hbar^2}U, \lambda = \tfrac{2m}{\hbar^2}E. \tag{47}$$

For equidistant mesh, the matrix B is symmetric and the eigenvectors are orthogonal.

4 α-Cluster nuclei ^{12}C, ^{16}O, ^{20}Ne, ^{24}Mg, ^{28}Si

4.1 Pairwise potentials and energies of the ground states for $N\alpha$ systems

The nuclear part of interaction between two α-particles may be represented as a potential involving a repulsive core for excluding forbidden (internal) states. The Ali–Bodmer (AB) potential version "a" [55]

$$V_{\alpha-\alpha}^{(\mathrm{N})}(r) = v_1\exp\left(-r^2/a_1^2\right) - v_2\exp\left(-r^2/a_2^2\right) \tag{48}$$

with $v_1 = 125$ MeV, $v_2 = 30.18$ MeV, $a_1 = 1.53$ fm, $a_2 = 2.85$ fm reproduces the s-wave α-α phase shift δ_0. The experimental and calculated s-wave α–α phase shifts are shown Fig. 2a. Coulomb repulsion of α-clusters was used in the form [55]

$$V_{\alpha-\alpha}^{(\mathrm{C})}(r) = \frac{4e^2}{r}\mathrm{erf}\,(\beta r)\,, \tag{49}$$

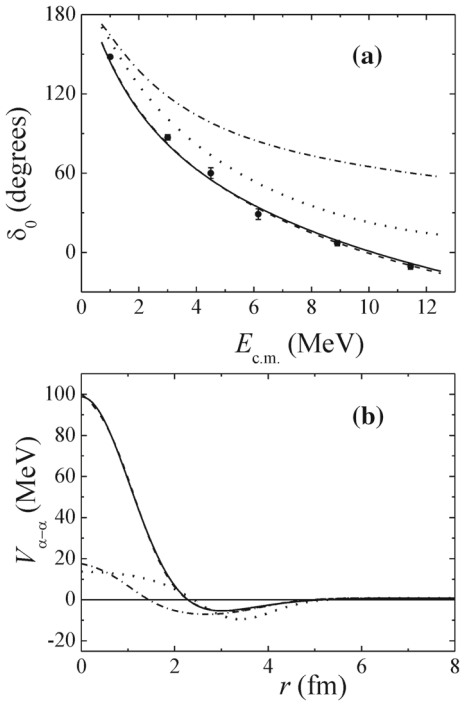

Fig. 2 **a** The experimental (dots) [55] and calculated (curves) s-wave α–α phase shifts: solid curve corresponds to the Ali–Bodmer potential "a" (48), dashed curve—to the similar DWS potential with parameters (54), (55), dotted curve—to the DWS potential with parameters (56), (57), dash-dotted curve—to the DWS potential with parameters (54), (58). **b** The Ali–Bodmer potential "a" (48) (solid curve) and the DWS potential with parameters: (54), (55) (dashed curve), (56), (57) (dotted curve), (54), (58) (dash-dotted curve)

where $\beta = 0.601$ fm^{-1} [36]. The total pairwise potential is the sum

$$V_{\alpha-\alpha}(r) = V^{(\rm N)}_{\alpha-\alpha}(r) + V^{(\rm C)}_{\alpha-\alpha}(r). \tag{50}$$

The plot of the Ali–Bodmer potential (48) is shown in Fig. 2b.

Calculations with the Ali–Bodmer potential result in the very small ground state energy for the 3α model of the ^{12}C nucleus [29]. When three or more α-particles (α-clusters) are close together, polarization and shell effects change the interaction between them [38]. This change was taken into account by including a three-body (3B) potential in the simple Gaussian form [36,38]

$$V_3(r) = S_3 \exp\left(-\frac{\rho^2\sqrt{3}}{4b_3^2}\right) = S_3 \exp\left(-\frac{\sqrt{3}}{b_3^2}\sum_{i=1}^{3} r_i^2\right) \tag{51}$$

with $b_3 = 2.58$ fm.

Modification of the pairwise potential may be another way of improving the description of the 3α system, more convenient for generalization to $N\alpha$ systems. For this purpose, we use the nuclear part of the potential for the zero orbital momentum in the form of the combination of two Woods–Saxon functions $f(r; B, a)$ (below we refer to it as double Woods–Saxon or DWS potential):

$$V^{(\rm N)}_{\alpha-\alpha}(r) = -U_{\alpha1} f(r; B_{\alpha1}, a_{\alpha1}) + U_{\alpha2} f(r; B_{\alpha2}, a_{\alpha2}), \tag{52}$$

$$f(r; B, a) = \left[1 + \exp\left(\frac{r-B}{a}\right)\right]^{-1}. \tag{53}$$

Potential (52) is similar to the Ali–Bodmer potential (48) for the set of parameters (see Fig. 2b)

$$U_{\alpha1} = 11.1 \text{ MeV}, B_{\alpha1} = 3.78 \text{ fm}, a_{\alpha1} = 0.54 \text{ fm}, \tag{54}$$
$$U_{\alpha2} = 115.34 \text{ MeV}, B_{\alpha2} = 1.14 \text{ fm}, a_{\alpha2} = 0.44 \text{ fm}. \tag{55}$$

Potential (52) with parameters

$$U_{\alpha1} = 29.0 \text{ MeV}, B_{\alpha1} = 3.73 \text{ fm}, a_{\alpha1} = 0.512 \text{ fm}, \tag{56}$$
$$U_{\alpha2} = 38.0 \text{ MeV}, B_{\alpha2} = 2.71 \text{ fm}, a_{\alpha2} = 0.512 \text{ fm} \tag{57}$$

was used in calculations of the ground state energies for $N\alpha$ systems with $N = 3, 4, 5, 6, 7$ using the FPI method in [56] and approximately reproduced the experimental values of the separation energy of an α-particle for the nuclei ^{16}O, ^{20}Ne, ^{24}Mg, ^{28}Si; errors were higher for the nuclei from ^{20}Ne to ^{28}Si. The s-wave α-α phase shifts are reproduced worse than for the Ali–Bodmer potential (48) and for the DWS potential with parameters (54)–(55) (see Fig. 2a).

We suppose that polarization and overlapping of α-clusters as well shell effects decrease the repulsive part of the α-α interaction in comparison with the Ali–Bodmer potential (48) and the DWS potential with parameters (54)–(55). Therefore, the parameter $U_{\alpha2}$ in the second (repulsive) term of the DWS potential (52), (53) must be modified to describe the ground state energies of $N\alpha$ systems. The energies of the 0^+ states for the ^{12}C nucleus (3α system) were calculated using the HSF method. The value of energy $E_0 = -7.27$ MeV for the ground state 0^+_1 coincided with the experimental value of energy of separation into three 3α particles $E_s = 7.27$ MeV (see, e.g., [3]); it was obtained with parameters

$$U_{\alpha2} = 26.76 \text{ MeV}, B_{\alpha2} = 1.07 \text{ fm}, a_{\alpha2} = 0.44 \text{ fm} \tag{58}$$

of the DWS potential for $n = 0, \ldots, 12$; $l_x = 0, \ldots, 12$; $K_{\max} = 48$; $N_s = 91$; $\rho_{\max} = n_p \Delta\rho = 30$ fm, $\Delta\rho = 0.2$ fm. The energy of the 0^+_2 state is equal to -0.967 MeV. The DWS α-α potential for the ^{12}C nucleus does not reproduce the s-wave α–α phase shifts δ_0 (see Fig. 2a). The difference between the potentials for α-α scattering and for α-systems may be explained by short times of α-α collisions, so that there is no time for polarization and shell effects to come into play.

The results of calculations of the propagator ${b_0}^{-1} \ln \tilde{K}_{\rm E}$ for the nuclei ^{12}C, ^{16}O, ^{20}Ne, ^{24}Mg, ^{28}Si are shown in Fig. 3a. The computational time for the FPI method grows

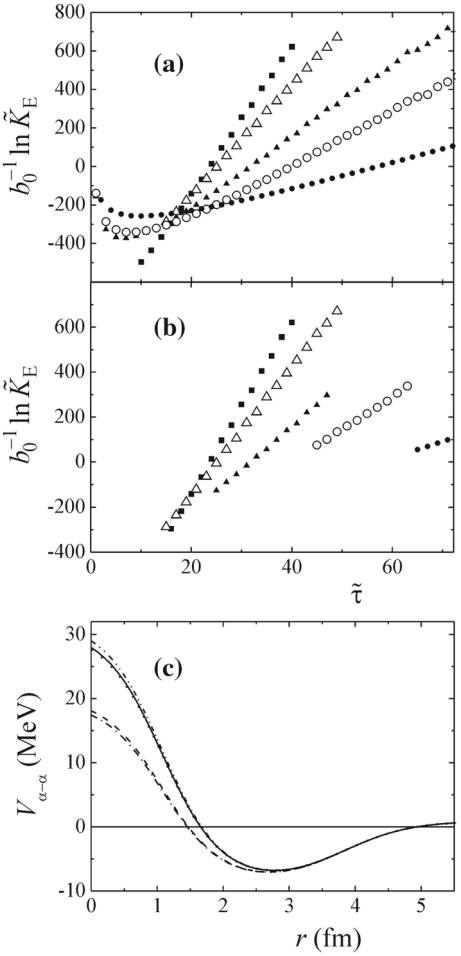

Fig. 3 **a** The results of calculations of the propagator $b_0{}^{-1} \ln \tilde{K}_E$ and **b** the linear parts of the graph of $b_0{}^{-1} \ln \tilde{K}_E$ as a function of $\tilde{\tau}$ for the nuclei ^{12}C (dots), ^{16}O (circles), ^{20}Ne (solid triangles), ^{24}Mg (empty triangles), ^{28}Si (squares) for grid spacing in imaginary time $\Delta\tilde{\tau} = 0.01$. **c** The DWS potentials $V_{\alpha-\alpha}(r)$ for ^{12}C (dash-dotted curve), ^{16}O (dashed curve), ^{20}Ne (dotted curve), ^{24}Mg (solid curve), ^{28}Si (dash-dot-dotted curve)

very slowly with the number of particles. The required time for parallel calculations of tens of millions of trajectories is approximately few hours on the Heterogeneous Cluster of the Joint Institute for Nuclear Research [52] and few tens of hours on ordinary laptops.

The linear parts of the graph of $b_0{}^{-1} \ln \tilde{K}_E$ as a function of $\tilde{\tau}$ are shown in Fig. 3b. The results of calculations of the ground state energy for the ^{12}C nucleus (3α system) using the FPI method demonstrated noticeable uncertainties (see Table 2). The plausible reason for it is the narrow linear part of the graph of $\tilde{K}_E$ as a function of τ near its inflection point. For a larger number of α-particles (α-clusters), the lengths of the linear parts of the graphs increase and uncertainties decrease. The results for the ground state energies are presented in Table 2. The graphs of α-α potentials $V_{\alpha-\alpha}(r)$ for the nuclei ^{12}C, ^{16}O, ^{20}Ne, ^{24}Mg, ^{28}Si are shown in Fig. 3c.

Table 2 Parameter $U_{\alpha 2}$ of the second (repulsive) term in the DWS potential (52) for α-cluster systems; other parameters are given in formulas (54), (58)

Nuclei	$U_{\alpha 2}$ (MeV)	$E_{s,\mathrm{exp}}$ (MeV)	$E_{s,\mathrm{calc}}$ (MeV)	Method
^{12}C (3α)	26.76	7.27	7.27	HSF
^{12}C (3α)	26.76	7.27	7.15 ± 0.10	FPI
^{16}O (4α)	27.50	14.44	14.40 ± 0.12	FPI
^{20}Ne (5α)	37.87	19.17	19.14 ± 0.15	FPI
^{24}Mg (6α)	38.22	28.48	28.43 ± 0.11	FPI
^{28}Si (7α)	39.37	38.47	38.54 ± 0.23	FPI

One can see that there are two different groups of the α-α potentials: first—for the nuclei ^{12}C, ^{16}O and second—for ^{20}Ne, ^{24}Mg, ^{28}Si. It may be explained by the difference in manifestations of polarization and shell effects in the nuclei with simple shapes (triangle for ^{12}C, tetrahedron for ^{16}O; see below) and in the nuclei with more complicated shapes, similar to a sphere (^{20}Ne, ^{24}Mg, ^{28}Si; see [56] and below).

4.2 2α System in self-consistent molecular orbit model

Antisymmetrization of nucleon wave functions in the 2α-cluster nuclei, such as Be and B isotopes, was taken into account in the AMD (antisymmetrized molecular dynamics) approach by Kanada-En'yo and Horiuchi [4,5]. This approach yielded the wave functions similar to those obtained in the molecular orbit model used in works [11–13]. In the two-center shell model [13], single-nucleon motion is described by the orbits in the mean field potential with two centers. For calculation of nucleon wave functions of ^{8}Be, we use a self-consistent shell model of atomic nuclei proposed in [57]. In this model, the potential energy of nucleons, depending non-linearly on the nucleon concentration n, is determined taking into account the Pauli Exclusion Principle. Nucleon–nucleon interaction $v(r)$, in particular its part corresponding to attraction, serves as a basis for choosing the family of functions $V(n)$. The function $V(n)$ is a superposition of two exponents that depend on the concentration via the quantity s having a dimension of length:

$$V(n) = -W_1 \exp\left[-\beta_1 s(n)\right] - W_2 \exp\left[-\beta_2 s(n)\right], \qquad (59)$$

where $W_1 = 172.8$ MeV, $W_2 = 45.55$ MeV, $\beta_1 = 1.641$ MeV, $\beta_2 = 0.438$ MeV,

$$s(n) = \left(\frac{3}{4\pi n}\right)^{1/3}. \qquad (60)$$

This nonlinear dependence for the mean field $V = V(n)$ of other nucleons on nucleon concentration $n(r)$ satisfies three conditions. The first condition

$$V\left[n(r)\right] \to 0, n(r) \to 0 \qquad (61)$$

requires absence of bound states of nucleons in a "loose" nucleus with internucleon distances exceeding the range of the nuclear force. A similar requirement in the opposite case

$$V\,[n(r)] \to \infty, n(r) \to \infty \tag{62}$$

is unnecessary because, due to the Uncertainty Principle, the kinetic energy of nucleons and their total energy automatically grow without any restrictions. The second condition of stability

$$\eta(n) = \left| \frac{n}{V} \frac{dV(n)}{dn} \right| \leq 1, \tag{63}$$

in accordance with the general mathematical principle of contraction mapping, is necessary for convergence of the iteration method of solving the nonlinear Schrödinger equation. Inequality (63) means that the magnitude of the relative change in the potential energy $|dV/V|$ does not exceed the relative change in the nucleon concentration $|dn/n|$ as the nucleon concentration varies. The third condition is the agreement of the solution obtained in the self-consistent shell model with the experimental data on nucleon separation energies along with the similarity of the self-consistent potential $V(n)$ for spherical nuclei with the well-known Woods–Saxon potential.

The self-consistent system of equations for two-center systems may be written in the cylindrical coordinate system. The Schrödinger equation for the two-component wave function of a neutron is

$$\left[-\frac{\hbar^2}{2m}\Delta + V(\rho,z) + i\frac{b}{2}\frac{1}{\rho}V_\rho\frac{\partial}{\partial\varphi}\right]\psi_{1\nu} + i\frac{b}{2}e^{-i\varphi}\left[i\left(V_\rho\frac{\partial}{\partial z} - V_z\frac{\partial}{\partial\rho}\right) - \frac{1}{\rho}V_z\frac{\partial}{\partial\varphi}\right]\psi_{2\nu} = \varepsilon_\nu\psi_{1\nu}, \tag{64}$$

$$\left[-\frac{\hbar^2}{2m}\Delta + V(\rho,z) - i\frac{b}{2}\frac{1}{\rho}V_\rho\frac{\partial}{\partial\varphi}\right]\psi_{2\nu} - i\frac{b}{2}e^{i\varphi}\left[i\left(V_\rho\frac{\partial}{\partial z} - V_z\frac{\partial}{\partial\rho}\right) + \frac{1}{\rho}V_z\frac{\partial}{\partial\varphi}\right]\psi_{1\nu} = \varepsilon_\nu\psi_{2\nu}. \tag{65}$$

Here m is the nucleon mass, $V_\rho \equiv \partial V/\partial\rho$, $V_z \equiv \partial V/\partial z$, $b = \frac{\kappa}{2}\frac{\hbar^2}{c^2m^2}$, c is speed of light, and κ is the spin-orbit coupling strength, the value $\kappa = 5$ was used. The method of numerical solution of the Schrödinger equation is described in the next subsection. Due to non-linearity of problem (59), (60) its numerical solution was obtained using an iteration scheme. Convergence of the iteration procedure is demonstrated in Fig. 4. The initial approximation for the two-center mean field V is the sum of two Woods–Saxon potential wells with distances R_{in} between their centers. The parameters of each Woods–Saxon potential well are the depth $V_0 = 55$ MeV, the width $r_0 = 2.25$ fm, and the diffuseness 0.7 fm. For large distances $R_{in} > 6$ fm, the energy of levels approximately corresponds to the experimental data on nucleon separation energies for ^{4}He, 20.6 MeV. For small values of $R_{in} < 5$ fm, the energy of levels is the same because the resulting self-consistent mean field and nucleon density do not depend on initial approximations.

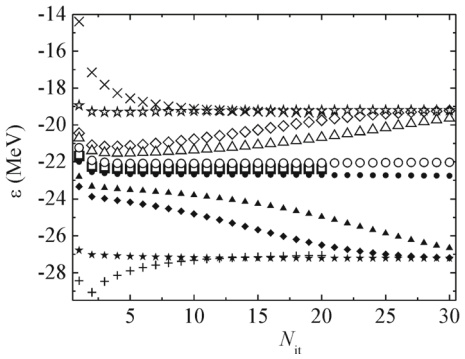

Fig. 4 Convergence of neutron energies ε for the two lower levels of the ^{8}Be nucleus in the iteration procedure of solution of the nonlinear Schrödinger equation for the initial approximation of the two-center mean field V as a sum of two Woods–Saxon potential wells with distances between their centers $R_{in} = 8$ fm (filled and empty squares), 6 fm (filled and empty circles), 5.25 fm (filled and empty triangles), 5 fm (filled and empty diamonds), 4 fm (filled and empty stars), 2 fm (direct and skew crosses); N_{it} is the number of iteration step

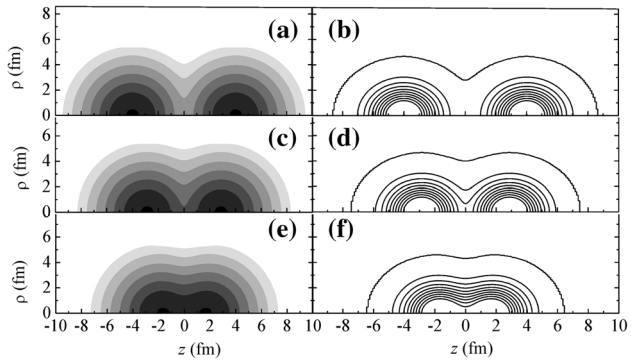

Fig. 5 The total nucleon density (shades of grey; logarithmic scale) for the ground state of the ^{8}Be nucleus in the self-consistent molecular orbit model (**a**, **c**, **e**) and landscapes of the self-consistent potentials (**b**, **d**, **f**) for the initial approximation of the two-center wave functions with distances between the centers of the Woods–Saxon potential wells $R_{in} = 8$ fm (**a**, **b**), 6 fm (**c**, **d**), 4 fm (**e**, **f**)

The total nucleon density for the ground state of the ^{8}Be nucleus in the self-consistent molecular orbit model and landscapes of the self-consistent potentials are shown in Fig. 5. The nucleon distributions have two peaks corresponding to the centers of α-clusters. Energies ε for the two lower neutron and proton levels of the ^{8}Be nucleus as a function of the distance $R_{\alpha-\alpha}$ between the peaks of the nucleon densities are shown in Fig. 6. In this model, the ^{8}Be nucleus, as system of four neutrons and four protons, may be in the stable self-consistent states only for $R_{\alpha-\alpha} > 3.4$ fm. Instability of the system when α-clusters approach each another may be an indication of strong repulsion in the $\alpha - \alpha$ interaction. The reason for repulsion in the semiempirical alpha-alpha

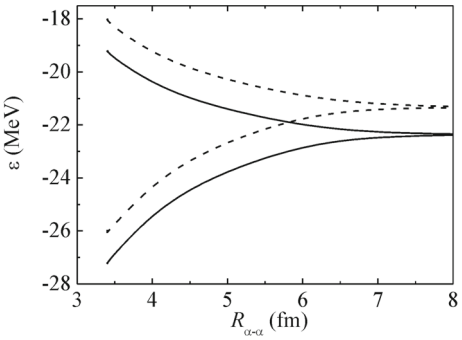

Fig. 6 Energies for two lower neutron (solid curves) and proton (dashed curves) levels E of the of the ^{8}Be nucleus as function of distances $R_{\alpha-\alpha}$ between the peaks of the nucleons densities

potential was demonstrated using the self-consistent shell model on the example of the ^{8}Be nucleus. The properties of the repulsive part of the potential may vary for different nuclei. These variations may be determined from comparing the theoretical results with experimental data.

We may say that the conditions where the alpha-cluster model may be applied to real nuclear systems are the existence of local peaks in the total nucleon density formed of neutron and protons pairs as in Fig. 5. In fact, in the calculation of the total nucleon density, antisymmetrization of nucleon wave functions may be taken into account via occupation of nucleon states using the Pauli Exclusion Principle in the self-consistent shell model for spherical or deformed nuclei. The role of nucleon density in formation of the internal structure with alpha clusters may be studied in the proposed self-consistent shell model owing to the nonlinear relationship (59), (60) between the nucleon density and the mean field.

4.3 Spatial structure of the ^{12}C nucleus in 3α model

For the ^{12}C nucleus (3α system) the physical distances proportional to the normalized Jacobi coordinates (24), (25) are

$$\mathbf{x} = \mathbf{r}_{\alpha_2} - \mathbf{r}_{\alpha_1},\ \mathbf{y} = \mathbf{r}_{\alpha_3} - \frac{1}{2}\left(\mathbf{r}_{\alpha_1} + \mathbf{r}_{\alpha_2}\right). \tag{66}$$

The potential landscapes for the total potential energies are shown in Figs. 7, 9. The convergence of the approximations of the HSF method is demonstrated in Tables 3, 4 for different α-α potentials, numbers of hyperradial equations, and values of mesh parameters. The satisfactory accuracy is achieved even for rather large mesh step $\Delta\rho \approx 0.6$ fm (Table 4). One may see that $\rho_{\max} = 20$ fm is large enough for the 0^+_1 state and $\rho_{\max} = 60$ fm is large enough for the 0^+_2 state.

The value of $S_3 = -152.2$ MeV used for calculations of the 3α system in [36] yielded the energy of the Hoyle state 0^+_2 0.3668877 MeV which was close to the experimental value 0.38 MeV [3]. The energy of the ground state 0^+_1 obtained in [36] was -9.300922 MeV which was rather far from the experimental value -7.27 MeV [3,38]. Thus, we may conclude that the strength of the three-body potential for the Hoyle state 0^+_2 is different from that for the ground state 0^+_1. The result of our calculations using splines interpolation is similar to the result of [36] for the 0^+_2 state, but differs from it for the 0^+_1 state. The strength of the repulsive core (the value of the parameter $U_{\alpha 2}$) for the Hoyle state 0^+_2 is different from that for the ground state 0^+_1 and is similar to that for the Ali–Bodmer (AB) potential for elastic scattering of α-particles. This fact may be explained by changes in the α-particles themselves (polarization and shell effects) in the compact 3α system as compared with free α-particles.

Using hyper-radial wave functions, we calculated the root-mean-square (rms) radius $\langle R^2\rangle = \langle\rho^2\rangle/4$ of the three-α system. We obtained 1.95 fm for the 0^+_1 state, this value is similar to result 1.78 fm [36] for AB+3B α-α potential (48), (51). The rms radii of the ^{12}C nucleus was determined in [36] as $R_{\rm rms} = \sqrt{\langle R^2\rangle + R^2_\alpha}$ with the rms radius of α-particle, $R_\alpha = 1.42$ fm. Our result $R_{\rm rms} = 2.41$ fm is also similar to result 2.28 fm [36].

We admit that for calculations of the 3α system, the HSF method is more precise and faster than the FPI method. The FPI method was used here only for the purposes of testing and estimating its uncertainty for the following study of the ground states of N-body systems with $4 \le N \le 7$, when the use of more accurate methods is very laborious.

The probability density for the ground state 0^+_1 of the ^{12}C nucleus calculated as a 3-body system 3α by the HSF method with cubic splines interpolation is shown in Fig. 7. The probability density is consistent with the potential landscape, which confirms the correctness of calculations. It is well known that the properties of the probability densities are determined by the potential landscape. The large values of the probability density are in the region where the energy of state exceeds the potential energy. The probability density is a rapidly decreasing function in the region where height of the barrier exceeds the energy of the state. We see a confirmation of this fact in Fig. 7 and below in all figures with the probability densities and potential landscapes.

The broad maximum of the probability density corresponds to the regular triangle with wide α-cluster clouds in its vertices. This result of the α-cluster model is similar to the result of the simple shell model of the deformed ^{12}C nucleus. The value of the quadrupole deformation $\beta_2 = -0.411 \pm 0.226$ [14] for the ^{12}C nucleus was obtained from the experimental value of quadrupole moment [58]. For a deformed nucleus with an axially symmetric surface described in the spherical coordinate system by the equation $R = R(\theta)$, the potential energy of a nucleon is usually

Table 3 The results of calculations of energies for the states 0_1^+ and 0_2^+ of the ^{12}C nucleus (3α system) within the HSF method with spline interpolation for AB+3B α-α potential (48), (51) and for different numbers of hyperradial equations and different values of mesh parameters: (i) $\Delta\rho = 0.2$ fm, $\rho_{\max}$= 20 fm; (ii) $\Delta\rho = 0.2$ fm, $\rho_{\max}$= 60 fm; (iii) $\Delta\rho = 0.2$ fm, $l_{x\max} = n_{\max} = 4$

	0_1^+ $S_3 = -152.2$ (MeV)	0_2^+ $S_3 = -152.2$ (MeV)	0_1^+ $S_3 = -132.5$ (MeV)	0_2^+ $S_3 = -132.5$ (MeV)
$l_{x\max}$	(i)			
$n_{\max}$				
2	−9.1891	0.840	−6.8921	1.4361
4	−9.5377	0.3879	−7.2414	0.9442
6	−9.5590	0.3384	−7.2653	0.8777
8	−9.5593	0.3311	−7.2658	0.8683
10	−9.5593	0.3285	−7.2658	0.8646
12	−9.5593	0.3278	−7.2658	0.8633
	(ii)			
2	−9.1891	0.8008	−6.8921	1.0879
4	−9.5377	0.3496	−7.2414	0.8412
6	−9.5590	0.2895	−7.2653	0.7444
8	−9.5593	0.2785	−7.2658	0.7197
10	−9.5593	0.2740	−7.2658	0.7150
$\rho_{\max}$ (fm)	(iii)			
12	−9.5244	2.2580	−7.2064	3.5306
16	−9.5377	0.6047	−7.2412	1.3274
20	−9.5377	0.3879	−7.2414	0.9442
24	−9.5377	0.3557	−7.2414	0.8663
30	−9.5377	0.3501	−7.2414	0.8450
60	−9.5377	0.3496	−7.2414	0.8412

Table 4 The results of calculations of energies for the states 0_1^+ and 0_2^+ of the ^{12}C nucleus (3α system) within the HSF method with spline interpolation for DWS α–α potentials (54), (58) and for different numbers of hyperradial equations and different values of mesh parameters: (i) $\Delta\rho = 0.2$ fm, $\rho_{\max} = 20$ fm; (ii) $\Delta\rho = 0.2$ fm, $\rho_{\max}$= 60 fm; (iii) $\Delta\rho = 0.2$ fm, $l_{x\max} = n_{\max} = 8$; (iv) $\rho_{\max} = 24$ fm and $l_{x\max} = 4$, $n_{\max} = 4$ for $U_{\alpha 2}$ =26.76 MeV, $\rho_{\max} = 60$ fm and $l_{x\max} = 8$, $n_{\max} = 8$ for $U_{\alpha 2}$ =61.5 MeV

	0_1^+ $U_{\alpha 2} = 26.76$ (MeV)	0_2^+ $U_{\alpha 2} = 26.76$ (MeV)	0_1^+ $U_{\alpha 2} = 61.5$ (MeV)	0_2^+ $U_{\alpha 2} = 61.5$ (MeV)
$l_{x\max}$	(i)			
$n_{\max}$				
2	−7.1728	−0.7136	−3.4147	1.3868
4	−7.2724	−0.9487	−3.6631	0.9462
6	−7.2735	−0.9695	−3.6709	0.8868
8	−7.2735	−0.9763	−3.6714	0.8661
10	−7.2735	−0.9771	−3.6715	0.8636
	(ii)			
2	−7.1728	−0.7136	−3.4115	0.9859
4	−7.2724	−0.9487	−3.6633	0.7416
6	−7.2728	−0.9695	−3.6712	0.5403
8	−7.2735	−0.9763	−3.6716	0.3807
$\rho_{\max}$ (fm)	(iii)			
12	−7.2049	−0.1047	−3.3912	2.8278
16	−7.2728	−0.8850	−3.6555	1.2014
20	−7.2735	−0.9763	−3.6714	0.8661
24	−7.2735	−0.9940	−3.6716	0.7449
30	−7.2735	−1.0002	−3.6716	0.5264
40	−7.2735	−1.0002	−3.6716	0.4075
60	−7.2735	−1.0002	−3.6716	0.3807

Table 4 continued

	0_1^+ $U_{\alpha 2} = 26.76$ (MeV)	0_2^+ $U_{\alpha 2} = 26.76$ (MeV)	0_1^+ $U_{\alpha 2} = 61.5$ (MeV)	0_2^+ $U_{\alpha 2} = 61.5$ (MeV)
$\Delta\rho$ (fm)	(iv)			
0.2	−7.2724	−0.9612	−3.6716	0.3807
0.3	−7.2682	−0.950	−3.6680	0.3881
0.6	−7.2657	−0.9531	−3.6488	0.3823
1.2	−7.1590	−0.9265	−3.5754	0.3871

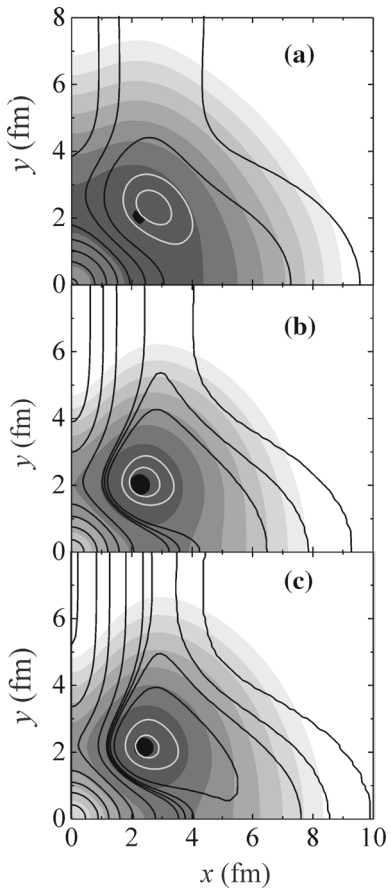

Fig. 7 The probability density (shades of grey; logarithmic scale) for the ground state 0_1^+ of the ^{12}C nucleus as a 3α system along with the potential landscape (curves) in the case of the distances (66) $\mathbf{x}\perp\mathbf{y}$ calculated by the HSF method for the DWS potential with parameters (54), (58), $U_{\alpha 2}$ =26.76 MeV (**a**) and AB+3B potential (48), (51) with parameters $b_3 = 2.58$ fm, $S_3 = -152.2$ MeV (**b**) and $S_3 = -132.5$ MeV (**c**)

represented in the Woods–Saxon form

$$U^{(\mathrm{WS})}(r, \cos\theta) = V_0 \left[1 + \exp\left(\frac{r - R(\theta)}{a^{(\mathrm{WS})}}\right)\right]^{-1}, \quad (67)$$

where the shape of a deformed nucleus with dimensionless deformation parameters β_2 is represented using the decomposition into spherical functions $Y_{\lambda 0}$ [59]

$$R(\theta) = \tilde{R}\left[1 + \beta_2 Y_{20}(\theta)\right], \quad (68)$$

$$\tilde{R} = R_0 \left(1 + \frac{3}{4\pi}\beta_2^2\right)^{-1/3}, \quad (69)$$

where $R_0 = r_0 A^{1/3}$, and A is the mass number. The nucleon states in the field of the axially deformed nucleus may be determined by solving the Schrödinger equation for two components ψ_1, ψ_2 of the spinor wave function in the cylindrical coordinates (ρ, φ, z):

$$\left[-\frac{\hbar^2}{2m}\Delta + U^{(\mathrm{WS})}(\rho, z) + i\frac{b}{2}\frac{1}{\rho}U_\rho^{(\mathrm{SO})}\frac{\partial}{\partial\varphi}\right]\psi_{1\nu} + i\frac{b}{2}e^{-i\varphi}\left[i\left(U_\rho^{(\mathrm{SO})}\frac{\partial}{\partial z} - U_z^{(\mathrm{SO})}\frac{\partial}{\partial\rho}\right) - \frac{1}{\rho}U_z^{(\mathrm{SO})}\frac{\partial}{\partial\varphi}\right]\psi_{2\nu} = \varepsilon_\nu\psi_{1\nu}, \quad (70)$$

$$\left[-\frac{\hbar^2}{2m}\Delta + U^{(\mathrm{WS})}(\rho, z) - i\frac{b}{2}\frac{1}{\rho}U_\rho^{(\mathrm{SO})}\frac{\partial}{\partial\varphi}\right]\psi_{2\nu} - i\frac{b}{2}e^{i\varphi}\left[i\left(U_\rho^{(\mathrm{SO})}\frac{\partial}{\partial z} - U_z^{(\mathrm{SO})}\frac{\partial}{\partial\rho}\right) + \frac{1}{\rho}U_z^{(\mathrm{SO})}\frac{\partial}{\partial\varphi}\right]\psi_{1\nu} = \varepsilon_\nu\psi_{2\nu}, \quad (71)$$

where the function $U^{(\mathrm{SO})}(r, \cos\theta)$ is

$$U^{(\mathrm{SO})}(r, \cos\theta) = V_0\left[1 + \exp\left(\frac{r - R(\theta)}{a^{(\mathrm{SO})}}\right)\right]^{-1}. \quad (72)$$

Here m is the nucleon mass, $U_\rho^{(\mathrm{SO})} \equiv \partial U^{(\mathrm{SO})}/\partial\rho$, $U_z^{(\mathrm{SO})} \equiv \partial U^{(\mathrm{SO})}/\partial z$, $b = \frac{\kappa}{2}\frac{\hbar^2}{c^2 m^2}$, c is speed of light, and κ is the spin-orbit coupling strength. It is necessary to supplement equations (70), (71) with the homogeneous boundary conditions at the cylinder surface ($\rho = \rho_0$, $z = z_0 < 0$, and $z = z_M > 0$) chosen in such a way that the distance from it to the surfaces of the nuclei significantly exceeds the range nuclear forces (about 1 fm). The resulting boundary-value problem has a discrete spectrum of energy eigenvalues $\varepsilon_\nu < 0$; values $\varepsilon_\nu \geq 0$ correspond to the continuous spectrum. Taking into account axial symmetry of the potential, the particular solutions are

$$\psi_{1\nu m_j} = (2\pi)^{-1/2} f_{1\nu m_j}(\rho, z)\exp\left[i(m_j - 1/2)\varphi\right],$$
$$\psi_{2\nu m_j} = (2\pi)^{-1/2} f_{2\nu m_j}(\rho, z)\exp\left[i(m_j + 1/2)\varphi\right], \quad (73)$$

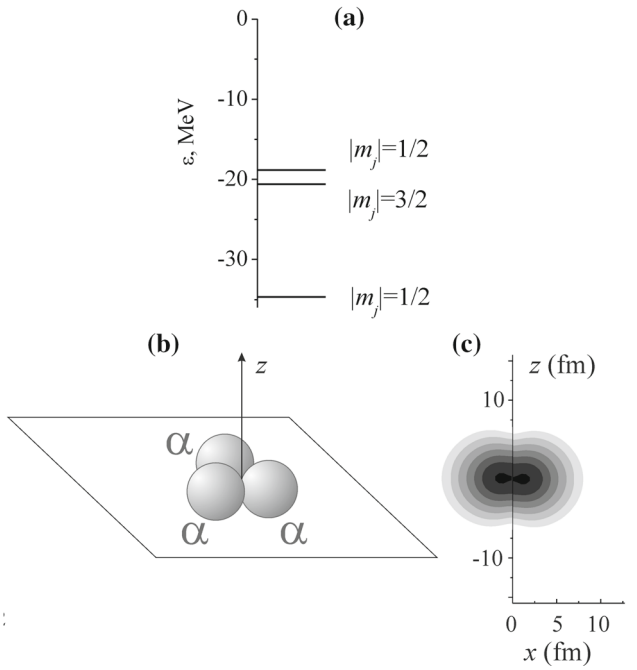

Fig. 8 Neutron level scheme (**a**) for the deformed ^{12}C nucleus obtained in the shell model of a deformed nucleus; the modules of the quantum numbers $|m_j|$ are shown. The regular triangle configuration in the alpha-cluster models (**b**) and the total neutrons probability density (logarithmic scale) for the deformed ^{12}C nucleus obtained in the shell model of a deformed nucleus (**c**)

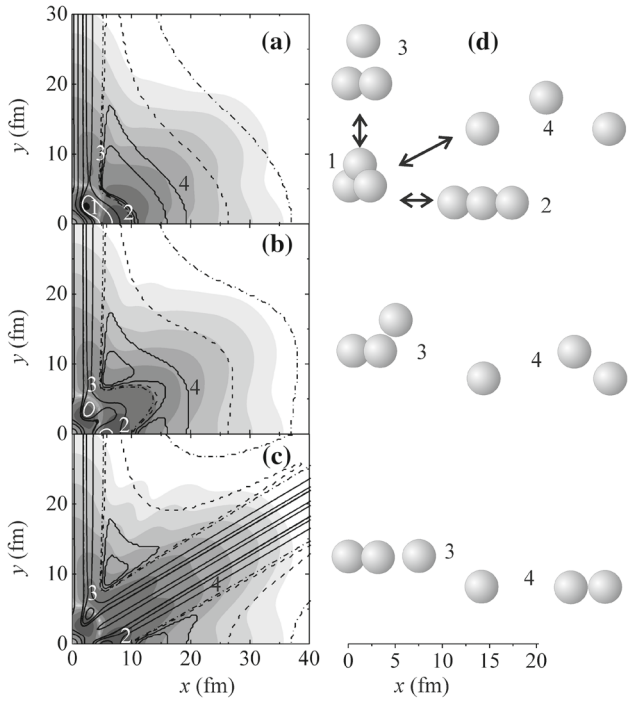

Fig. 9 The probability density (shades of grey; logarithmic scale in the range of 7 orders of magnitude) for the excited state 0_2^+ (Hoyle state) of ^{12}C in 3α model calculated by the HSF method along with the potential landscape (level curves, particularly dash-dotted curves for 0.8 MeV, dashed curves for 1 MeV, white curves for -10 MeV) for the distances (66) $\mathbf{x}\perp\mathbf{y}$ (**a**), for angle $\theta = \pi/4$ between vectors $\mathbf{x}$, $\mathbf{y}$ (**b**), and for $\mathbf{x} \parallel \mathbf{y}$ (**c**) with the 3D models of some configurations (**d**). The regular triangle configuration 1, the linear configuration 2, and the compact dinuclear configurations 3 (^{8}Be + α-cluster) are the most probable; the sparse configurations 4 are of very small probability. The arrows show oscillatory relative motion of α-clusters between the compact regular triangle configuration 1 and the linear dinuclear configurations 2, 3 near the top of the multi-dimensional Coulomb barrier. The calculations were done with the DWS potential with parameters (54), (58) and $U_{\alpha 2} = 61.5$ MeV

where $m_j = -j, -j+1, \ldots, j$ is the quantum number of the angular-momentum projection onto the nuclear symmetry axis Oz. The probability density P in cylindrical coordinates for neutron levels with quantum numbers ν, m_j is

$$P = \left|\psi_{1\nu m_j}\right|^2 + \left|\psi_{2\nu m_j}\right|^2 . \tag{74}$$

For solving Schrödinger equations (70), (71), we used the method based on expansion of functions f_1 and f_2 into a series of Bessel functions proposed in [60]. The calculations within the shell model of the deformed ^{12}C nucleus yielded energies ε_ν of the upper occupied level which were approximately equal to the experimental neutron separation energies 18.72 MeV taken with opposite signs [3]. The resulting neutron level scheme $\varepsilon_\nu\left(|m_j|\right)$ is shown in Fig. 8a. The parameters of the shell model are $V_0 = 60.3$ MeV, $r_0 = 1.2$ fm, $a^{(\mathrm{WS})} = 0.6$ fm, $\kappa = 38$. The Pauli Exclusion Principle states that no more than two neutrons with $m_j = \pm|m_j|$ can occupy each level; there are three occupied levels with quantum numbers $m_j = \pm 1/2, \pm 3/2, \pm 1/2$. The total neutrons probability density (and similar for protons) obtained in the shell model of a deformed nucleus is similar to the oblate total nucleon distribution for the regular triangle configuration in the alpha-cluster model.

Examples of the probability density for the excited state 0_2^+ (Hoyle state) of ^{12}C calculated by the HSF method along with the potential landscapes for the total potential energies are shown in Fig. 9. The potential (Coulomb) barrier surrounds the region of the ^{12}C nucleus; the level curves for 0.8 and 1 MeV are shown in Fig. 9. The height of the barrier exceeds the positive 3-body energy of the 0_2^+ state everywhere, except the narrow ravines for the breakup channel ^{8}Be+^{4}He. The module of the wave function of the quasi-stationary 0_2^+ state is rapidly decreasing function in the region where the height of the barrier exceeds the energy of the 0_2^+ state (0.4 MeV, for results in Fig. 9). Therefore the zero boundary condition at a large value $\rho_{\max}$ is a reasonable approximation for calculations using the HSF method. The 3-body energy depends weakly on the choice of $\rho_{\max}$ at $\rho_{\max} > 40$ fm. Of course, the result for the wave function will be incorrect in the narrow ravines for the breakup

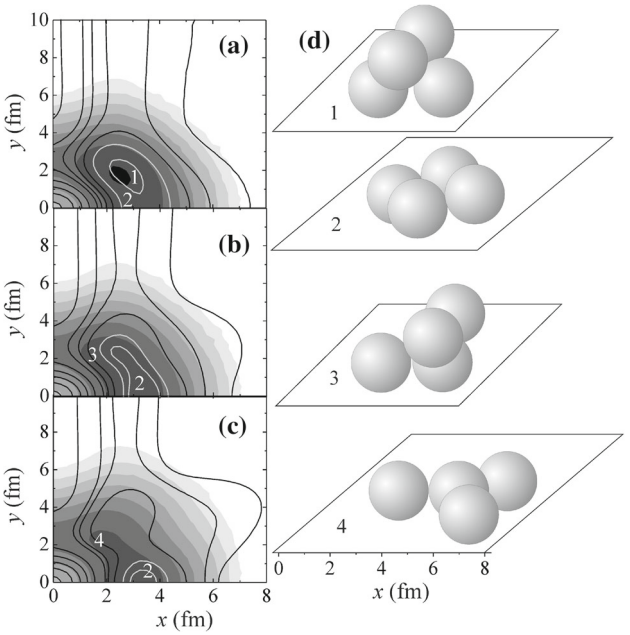

Fig. 10 Topography (shades of grey; logarithmic scale) of the propagator $\tilde{K}_{\rm E}$ (20), i.e., the probability density for the ground state of the ^{16}O nucleus as a 4α system calculated by the FPI method along with the potential landscape (curves) for the distances (75) $\mathbf{x}\perp\mathbf{y}$, $x =$ and $\mathbf{x}\perp\mathbf{z}$ (**a**), for angle $\theta = \pi/4$ between vectors $\mathbf{x}$, $\mathbf{z}$ (**b**), and for $\mathbf{x} \parallel \mathbf{z}$ (**c**) with the 3D models of some configurations (**d**). The tetrahedron configuration 1 is the most probable; the square configuration 2 is of considerably lower probability; the dinuclear configurations 3, 4 ($\alpha + ^{12}$C) are even less probable. The calculations were done for the DWS potential with parameters (54), (58) and $U_{\alpha 2}$ from Table 2

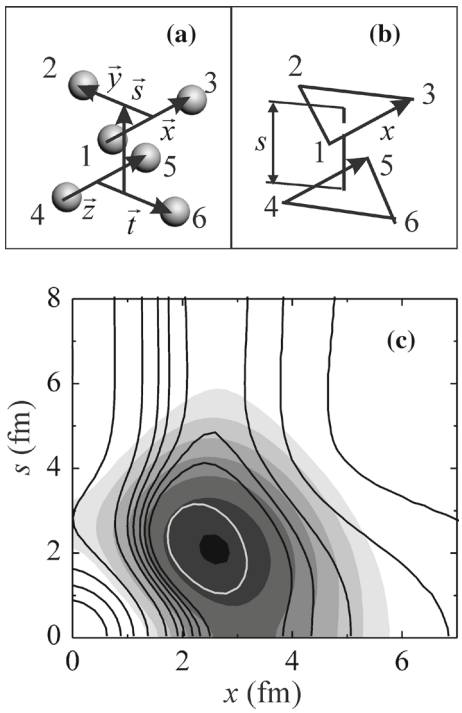

Fig. 11 **a** Five physical distances proportional to the normalized Jacobi coordinates for the ^{24}Mg nucleus (6α-system) in the case of $\mathbf{x}\perp\mathbf{y}$, $\mathbf{y}\perp\mathbf{s}$, $\mathbf{x} \parallel \mathbf{z}$, $\mathbf{y} \parallel \mathbf{t}$ for the shape of a pair of equal regular triangles with α-clusters in their vertices (**b**). **c** The probability density (shades of grey; logarithmic scale) for this configuration of the ground state of the ^{24}Mg (6α) nucleus along with the potential landscape (curves). The calculations were done for the DWS potential with parameters (54), (58) and $U_{\alpha 2}$ from Table 2

channel ^{8}Be+^{4}He, but in the central area of the ^{12}C nucleus the probability density may be used for studying the spatial structure of the Hoyle state. The probability density is consistent with the potential landscape, which confirms the correctness of calculations. For the Hoyle state, there are two probable separate configurations: regular triangle configuration and linear dinuclear configuration (^{8}Be + α-cluster). The Hoyle state may correspond to oscillatory relative motion of α-clusters between the compact regular triangle configuration and the linear dinuclear configuration near the top of the multi-dimensional Coulomb barrier.

4.4 Spatial structures of the ^{16}O and ^{24}Mg nuclei in 4α and 6α models

For the ^{16}O nucleus (4α system), the physical distances proportional to the normalized Jacobi coordinates are

$$\begin{aligned} &\mathbf{x} = \mathbf{r}_{\alpha_2} - \mathbf{r}_{\alpha_1},\ \mathbf{y} = \mathbf{r}_{\alpha_4} - \mathbf{r}_{\alpha_3}, \\ &\mathbf{z} = \tfrac{1}{2}\left(\mathbf{r}_{\alpha_4} + \mathbf{r}_{\alpha_3}\right) - \tfrac{1}{2}\left(\mathbf{r}_{\alpha_2} + \mathbf{r}_{\alpha_1}\right). \end{aligned} \tag{75}$$

Examples of the probability density for the ground state of the ^{16}O nucleus calculated as a 4-body system by the FPI method for Jacobi vectors $\mathbf{x}\perp\mathbf{y}\perp\mathbf{z}$ are shown in Fig. 10. An evident result is that the broad maximum of the probability density corresponds to the tetrahedron configuration with wide α-cluster clouds in its vertices. This result of the α-cluster model is similar to the result of the simple shell model of the ^{16}O nucleus. The square configuration and the dinuclear configuration ($\alpha + ^{12}$C) are of considerably lower probability.

For the ^{24}Mg nucleus (6α system), the physical distances proportional to the normalized Jacobi coordinates are shown in Fig. 11a. The probability density distribution for the ground state is shown in Fig. 11c for the shape of a pair of equal regular triangles with α-clusters in their vertices (Fig. 11b). The sides of the triangles are equal to x and the distance between the centers of the triangles is equal to s. The probability density is consistent with the potential landscape, which confirms the correctness of calculations. The most probable configuration is a pair of regular triangles. This configuration may be represented as a combination of two carbon clusters (3α + 3α).

Table 5 Parameters of the Afnan–Tang nucleon–nucleon potentials (76), (77) for triplet p–n and singlet p–n, p–p systems

Potential	V_{t1} (MeV)	V_{t2} (MeV)	V_{t3} (MeV)	State, system
S3 [61]	1000.0	−326.7	−43.0	Triplet p–n
S4 [61]	600.0	−70.0	−27.6	Triplet p–n
SX [63]	500.0	−102.0	−2.0	Triplet p–n
S3 [61]	1000.0	−166.0	−23.0	Singlet p–n, p–p
S4 [61]	880.0	−70.0	−21.0	Singlet p–n, p–p
SX [63]	500.0	−102.0	−2.0	Singlet p–n, p–p
Potential	β_{t1}	β_{t2}	β_{t3}	State,
	(fm^{-2})	(fm^{-2})	(fm^{-2})	System
S3 [61]	3.0	1.05	0.6	Triplet p–n
S4 [61]	5.5	0.5	0.38	Triplet p–n
SX [63]	11.41	0.625	0.141	Triplet p–n
S3 [61]	3.0	0.8	0.40	Singlet p–n, p–p
S4 [61]	5.4	0.64	0.48	Singlet p–n, p–p
SX [63]	4.15	0.625	0.141	Singlet p–n
SX [63]	3.92	0.625	0.141	Singlet p–p

5 Spatial structures of the nuclei ^{9}Be, ^{10}Be, ^{10,11}B, ^{10,11}C in 2α model

5.1 Nucleon–nucleon potentials

The nuclear part of the nucleon–nucleon interaction may be described by the effective pairwise central soft-core Afnan–Tang potential [61] for a triplet state

$$V_t(r) = \sum_{k=1}^{3} V_{ti} \exp(-\beta_{ti} r^2) \tag{76}$$

and for a singlet state

$$V_s(r) = \sum_{k=1}^{3} V_{si} \exp(-\beta_{si} r^2). \tag{77}$$

The values of the parameters of potentials (76), (77) depend on the total isospin of a two-nucleon system; they are given in [61] and in Table 5. The proton–neutron triplet potentials $V_t(r)$ named as S3 and S4 in [61] lead to the value of the ground state energy for the ^{2}H nucleus, −2.22 MeV. This result may be easily obtained using the method based on splines interpolation of the radial wave function (46), (47), e.g., for $n_p = 200$, $\Delta r = 0.1$ fm. Potentials S3 and S4 satisfactorily reproduce the experimental s-wave phase shifts δ_0 [62]. The experimental and calculated s-wave triplet p–n and singlet p–n, p–p phase shifts are shown in Fig. 12.

The s-wave singlet phase shifts for proton-neutron scattering are satisfactorily reproduced (see Fig. 12b) with the potential named below as SX; its parameters are given in Table 5. This singlet potential (77) SX was used in [63,64] for description of neutron-neutron interaction in the nuclei ^{6,7,9,11}Li [63], ^{6,7,9,10}Be [64]. The proton–neutron triplet potentials $V_t(r)$ SX also lead to the experimental value of the ground state energy for the ^{2}H nucleus, −2.22 MeV. The graphs of the potentials S3, S4, and SX are shown in Fig. 13.

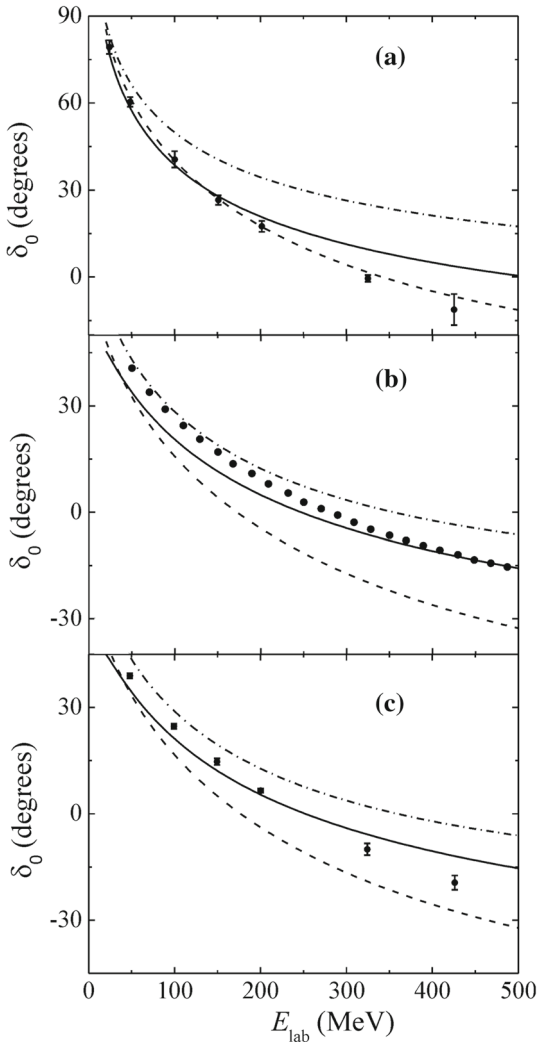

Fig. 12 The experimental (dots) [62] and calculated (curves) phase shifts for s-wave (**a**) triplet p–n, (**b**) singlet p–n, and (**c**) p–p. Curves are the results obtained with the Afnan–Tang potentials (76), (77) S4 (solid curves), S3 (dashed curves), and the SX potentials used in [63,64] (dash-dotted curves). The parameters of the potentials are given in Table 5

The experimental values of the separation energy for the nuclei ^{3}H and ^{3}He are 8.48 and 7.72 MeV, respectively. Variational calculations with the effective spin-independent nucleon-nucleon potential of the form

$$V_e(r) = \frac{1}{2}\left[V_t(r) + V_s(r)\right] \tag{78}$$

lead to the upper bound of the ground-state energy −6.56 MeV and the ground state energy about −6.7 MeV [61]. Similar

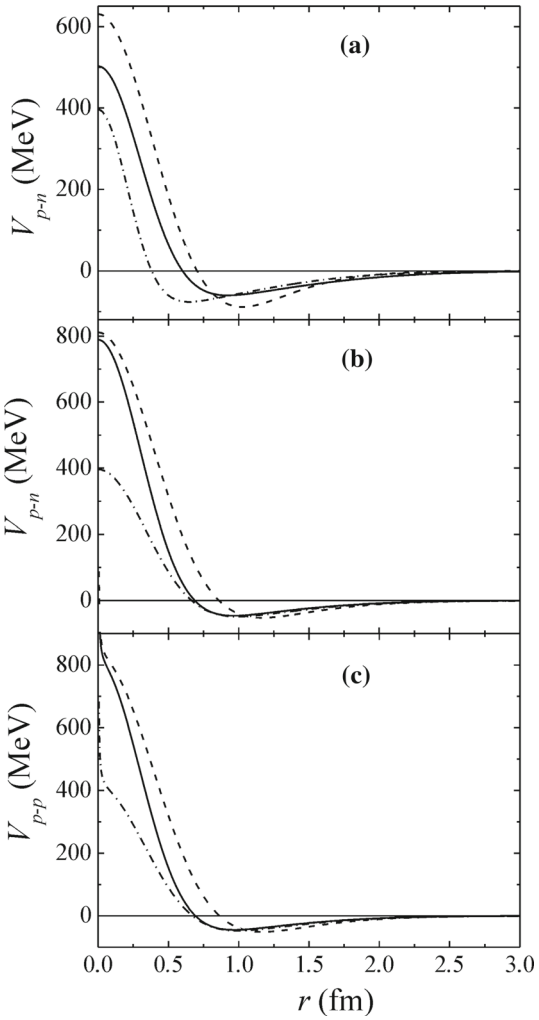

Fig. 13 The graphs of the Afnan–Tang potentials (76), (77) S4 (solid curves), S3 (dashed curves), and the potential SX (dash-dotted curves) for **a** triplet state of the system $p+n$, **b** singlet state of the system $p+n$, **c** singlet state of the system $p+p$. The parameters of the potentials are given in Table 5

results were obtained in several works using different methods: −6.68 MeV [44], −6.6953 MeV [65], −6.64 MeV [66], −6.69 MeV [67]. The results of the HSF calculations for the effective nucleon–nucleon potential (78) and the potential energy of the 3-body system $p+n+n$

$$V_{p,n,n} = V_e\left(\left|\mathbf{r}_{n_2}-\mathbf{r}_{n_1}\right|\right) + V_e\left(\left|\mathbf{r}_p-\mathbf{r}_{n_1}\right|\right) + V_e\left(\left|\mathbf{r}_p-\mathbf{r}_{n_2}\right|\right) \tag{79}$$

are given in Table 6. The ground state energy for spin-independent potential energy $V_{p,n,n}$ (79) is about −6.7 MeV as in the above-mentioned Refs.

In the model with spin-dependent potentials the potential energy of the 3-body system ^{3}H $(p+n+n)$ may be represented as

Table 6 The results of calculations of energy (MeV) for the ground states of the ^{3}H nucleus within the HSF method with spline interpolation for S3 potentials (76), (77) with parameters from Table 5 and different numbers of hyperradial equations with mesh parameters $\Delta\rho = 0.1$ fm, $\rho_{\max}$=15 fm for spin-independent potential energy $V_{p,n,n}$ (79) and $\Delta\rho = 0.2$ fm, $\rho_{\max}$=20 fm for spin-dependent potential energy $V_{p,n,n}$ (80)

$l_{x\max}$	$n_{\max}$	for $V_{p,n,n}$ (79)	for $V_{p,n,n}$ (80)
2	6	−5.4008	−4.4975
4	8	−6.3075	−5.2699
6	10	−6.5626	−5.5279
8	12	−6.6408	−5.6277
10	14	−6.6655	−5.70

Table 7 The results of calculations of the ground state energy (MeV) of the ^{3}H and ^{3}He nuclei for spin-dependent potential energies within the HSF method with spline interpolation for SX potentials (76), (77) with parameters from Table 5 and different numbers of hyperradial equations with mesh parameters $\Delta\rho = 0.1$ fm, $\rho_{\max}$=15 fm

$l_{x\max}$	$n_{\max}$	^{3}H	^{3}He
2	6	−8.0848	−7.3506
4	8	−8.3504	−7.6143
6	10	−8.4301	−7.6946
8	12	−8.4581	−7.7233
10	14	−8.4692	−7.7348

$$V_{p,n,n} = V_s^{(n,n)}\left(\left|\mathbf{r}_{n_2}-\mathbf{r}_{n_1}\right|\right) + V_s^{(p,n)}\left(\left|\mathbf{r}_p-\mathbf{r}_{n_1}\right|\right) + V_t^{(p,n)}\left(\left|\mathbf{r}_p-\mathbf{r}_{n_2}\right|\right). \tag{80}$$

The potential energy of the 3-body system ^{3}He $(p+n+p)$ may be represented in a similar form with addition of the Coulomb repulsion for protons. The results of calculations of the ground state energy of the ^{3}H nucleus for spin-dependent potential energy $V_{p,n,n}$ (80) are given in Table 6 for the S3 potentials and in Table 7 for the SX potentials. The results of similar calculations of the ground state energy of the ^{3}He nucleus for the SX potentials are given in Table 7. The results for the SX potentials coincide with the experimental values.

The probability density for the ^{3}H nucleus is shown in Fig. 14. We used the set of the physical distances proportional to the normalized Jacobi coordinates (24), (25):

$$\mathbf{x} = \mathbf{r}_p - \mathbf{r}_{n_1},\ \mathbf{y} = \mathbf{r}_{n_2} - \frac{1}{2}\left(\mathbf{r}_{n_1}+\mathbf{r}_p\right), \tag{81}$$

where the masses of protons and neutrons are considered to be equal because the difference between them is small. The narrow maximum of the probability density corresponds to an isosceles triangle with wide nucleons clouds in its vertices. The space structure of the ^{3}H nucleus is similar to a compressed deuteron cluster in the cloud of the second neutron.

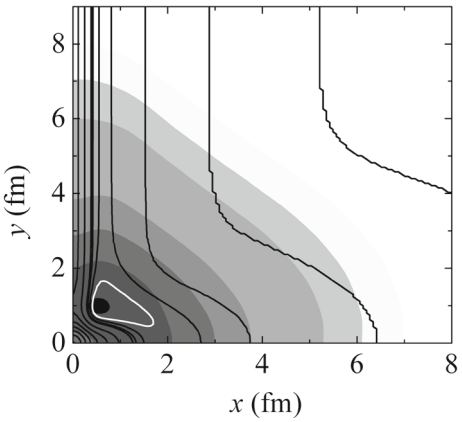

Fig. 14 The probability density (shades of grey; logarithmic scale) for the ground state of the ^{3}H nucleus along with the potential landscape (curves) for $\mathbf{x}\perp\mathbf{y}$. The calculations were done for the spin-dependent potential energy (80) within the HSF method with spline interpolation for SX potentials (76), (77) with parameters from Table 5

Just as for $N\alpha$ systems, the ground state energy may closer to the experimental value if a repulsive core of the effective pairwise potential is decreased in comparison with the potential used for description of particle scattering. Below we use the potentials SX and DWS with parameters (56), (57) to calculate of the ground state energies for the nuclei ^{10}Be, ^{10,11}B, ^{10,11}C.

5.2 α-Nucleon potentials and spatial structure of the ^{9}Be nucleus

The need of modification of pairwise potentials for N-body systems leads to using effective α-nucleon pseudopotentials $V_{\alpha-n}$ and $V_{\alpha-p}$ in calculations. The pseudopotentials do not take into account the data on phase shifts (e.g., [68]), but their forms are similar to α–α and nucleon–nucleon potentials. The parameters of the pseudopotentials were determined from the condition of equality of the calculated and experimental values of the ground state energies for systems α-cluster + nucleons, in particular, for the nuclei: ^{6}He [48], ^{6,7}Li [63], ^{6,7}Be [64].

For α-cluster nuclei with two or three outer nucleons the parameters of α-nucleon pseudopotentials depend on the choice of the form and the parameters of nucleon–nucleon potentials. In [63,64], this pseudopotential was chosen as a combination

$$V_{\alpha-N}(r) = -U_1 f(r; B_1, a_1) + U_2 f(r; B_2, a_2) - U_3 f(r; B_3, a_3) f(r; B_4, a_4). \quad (82)$$

A similar form with only two first terms of the α-nucleon interaction was used in [23] for calculations of the ^{6}Li nucleus. The values of the parameters of α-nucleon pseudopotential (82) are given in Table 8 [63,64]. The pseudopotential $V_{\alpha-p}(r)$ includes the Coulomb interaction approximated as the interaction of a point charge with a uniformly charged sphere. The graphs of the pseudopotentials $V_{\alpha-n}(r)$, $V_{\alpha-p}(r)$ are shown in Fig. 15. Expression (82) has the meaning of a pseudopotential of strong interaction between an α-cluster and a neutron or a proton, similar to the pseudopotential [69] used in metal physics to describe the interaction between external electrons (from the conduction band) and atomic cores. The second term in (82) is positive due to the presence of repulsive cores in the potentials of nucleon–nucleon interaction and as consequence of the Pauli Exclusion Principle. The energy of the ground state in the core-nucleon system is close to that of the uppermost occupied level in the nuclear shell model. In this case, the nucleon states of the nuclear core corresponding to underlying levels ($1s$, in spherical shell model) are excluded (forbidden).

Table 8 Parameters of α-nucleon pseudopotential (82)

i	U_i (MeV) (i)	U_i (MeV) (ii)	B_i (fm)	a_i (fm)
1	64.8	64.8	1.95	0.25
2	55.8	55.8	1.22	0.3
3	126.0	107.13	0.9	0.5
4			2.7	1.

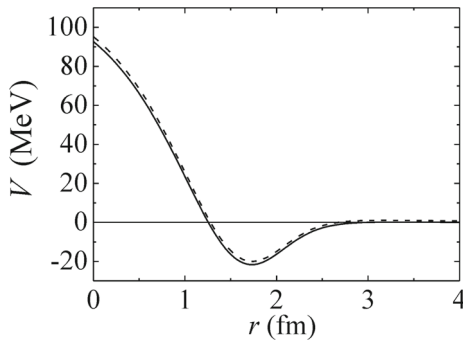

Fig. 15 The graphs of pseudopotentials (82) with parameters from Table 8 (with value (i) of U_3): $V_{\alpha-n}(r)$ (solid line) and $V_{\alpha-p}(r)$ (dashed line)

The α-nucleon pseudopotentials, independent from the choice of nucleon–nucleon potentials, may be determined by studying the simplest stable α-cluster nucleus with only one outer neutron, that is the ^{9}Be nucleus (the ^{5}He nucleus is unstable). In the calculations of the ^{9}Be nucleus we used α–α potentials (52) with parameters (54), (55) corresponding to interaction of the scattering α-particles, because polarization and shell effects in the ^{9}Be nucleus are less important than in the ^{12}C nucleus. For the ^{9}Be $(\alpha+\alpha+n)$ nucleus, the physical distances proportional to the normalized Jacobi coordinates (24), (25) are

Table 9 The results of calculations of the ground state energy (MeV) for ^{9}Be nucleus ($2\alpha + n$ system) within the HSF method with spline interpolation for DWS α–α potential (54), (55) together with α-neutron pseudopotentials (82) with parameters from Table 8 (with value (ii) of U_3) and for different numbers of hyperradial equations with mesh parameters $\Delta\rho = 0.2$ fm, $\rho_{\max}$=20 fm

$l_{x\max}$	$n_{\max}$	$E_{s,\mathrm{calc}}$	$l_{x\max}$	$n_{\max}$	$E_{s,\mathrm{calc}}$
2	2	−0.83556	6	8	−1.54727
4	4	−1.36632	6	10	−1.55502
6	6	−1.51832	6	12	−1.55769
8	8	−1.55780	6	14	−1.55853
10	10	−1.56902	6	16	−1.55882
12	12	−1.57259	6	18	−1.55894
14	14	−1.57377	6	20	−1.55899

$$\mathbf{x} = \mathbf{r}_{\alpha_2} - \mathbf{r}_{\alpha_1}, \mathbf{y} = \mathbf{r}_n - \frac{1}{2}\left(\mathbf{r}_{\alpha_2} + \mathbf{r}_{\alpha_1}\right). \tag{83}$$

For calculations of the 3-body system ($2\alpha + n$), we used the precise HSF method and the FPI method to estimate its uncertainties. The separation energy for the ^{9}Be($2\alpha + n$) nucleus is $E_{s,\mathrm{exp}}$ =1.572 MeV [3]. The results of calculations of the energy of the ground state for the system ($2\alpha+n$), $E_0 \approx -E_{s,\mathrm{exp}}$, for the parameters from Table 8 (with value (ii) of U_3) are given in Table 9. α-nucleon pseudopotentials (82) with two values of the parameter $U_3 = 126$ MeV and $U_3 = 107.13$ MeV are similar.

The results of calculations of the propagator $b_0{}^{-1} \ln \tilde{K}_\mathrm{E}$ for pseudopotentials (82) with $U_3 = 107.13$ MeV are shown in Fig. 16a. The result of calculations of the ground state energy using the FPI method, $E_0 \approx 0.53 \pm 0.1$ MeV, is rather different from the exact value because it is near the continuum spectrum. In this case, the propagator $K_\mathrm{E}(\mathbf{q}, \tau; \mathbf{q}, 0)$ may be represented in the following asymptotic form:

$$K_\mathrm{E}(\mathbf{q}, \tau; \mathbf{q}, 0) \to |\psi_0(\mathbf{q})|^2 \exp\left(-\frac{E_0\tau}{\hbar}\right) + |\Phi(\mathbf{q})|^2 + \cdots, \ \tau \to \infty, \tag{84}$$

where $|\Phi(\mathbf{q})|^2$ is a sum of the contributions of continuum spectrum states with $E \approx 0$. The approximate probability density of the ground state $|\psi_0(\mathbf{q})|^2$ may be calculated as the difference

$$K_\mathrm{E}(\mathbf{q}, \tau_2; \mathbf{q}, 0) - K_\mathrm{E}(\mathbf{q}, \tau_1; \mathbf{q}, 0) \approx |\psi_0(\mathbf{q})|^2 \exp\left(-\frac{E_0(\tau_2-\tau_1)}{\hbar}\right). \tag{85}$$

The examples of the propagators $\tilde{K}_\mathrm{E}$ for two values of τ, $\tilde{\tau} = 30$, $\tilde{\tau} = 45$, and difference (85) are shown in Fig. 16b–d. The approximate probability density of the ground state corresponds to the distribution in Fig. 16d. The distributions in Fig. 16b, c correspond to the excited breakup (or collision) states ^{4}He + ^{5}He.

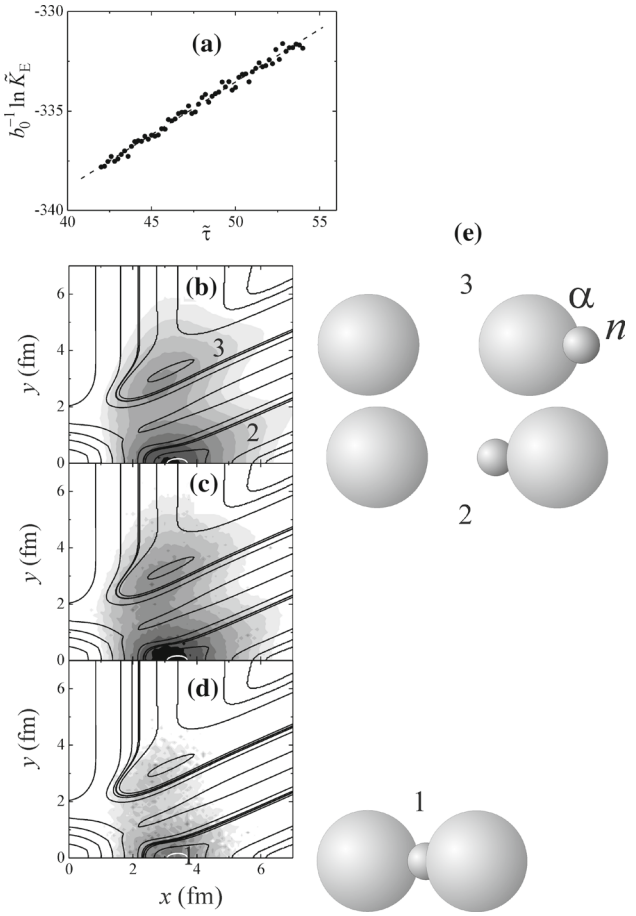

Fig. 16 **a** Dependence of the normalized logarithm of propagator $\tilde{K}_\mathrm{E}$ (23) on imaginary time τ for the ^{9}Be nucleus. The propagators $\tilde{K}_\mathrm{E}$ (shades of grey; logarithmic scale) along with the potential landscape (curves) in the case of the distances (83) $\mathbf{x} \parallel \mathbf{y}$ for two values of τ: $\tilde{\tau} = 30$ (**b**), $\tilde{\tau} = 45$ (**c**), and difference (85) (**d**). Calculations by the FPI method were made for DWS α–α potential (54), (55) together with α-neutron pseudopotentials (82) with parameters from Table 8 ($U_3 = 107.13$ MeV). **e** The examples of the positions of a neutron (small sphere) and α-clusters (large spheres). Configuration 1 is the most probable and corresponds to the ground state; configurations 2 and 3 correspond to the excited breakup (or collision) states ^{4}He + ^{5}He

The examples of the probability density for the ground state of the ^{9}Be nucleus calculated as a 3-body system $2\alpha+n$ by the HSF method with cubic spline interpolation are shown in Fig. 17. The narrow maximum of the probability density and $\tilde{K}_\mathrm{E}$ in Figs. 16d and 17a, b correspond to the most probable configuration with a valence neutron between α-clusters ($\alpha+n+\alpha$) in the ground state of the ^{9}Be nucleus. We note that for the linear configuration $\mathbf{x} \parallel \mathbf{y}$, HSF dispersion (30) for the wave function has very slow convergense at $\theta = 0$ because $P_l(1) = 1$.

Below we use α-nucleon pseudopotential (82) with parameters from Table 8 (with value (i) of U_3) and the potentials SX and DWS with parameters (56), (57) to calculate the

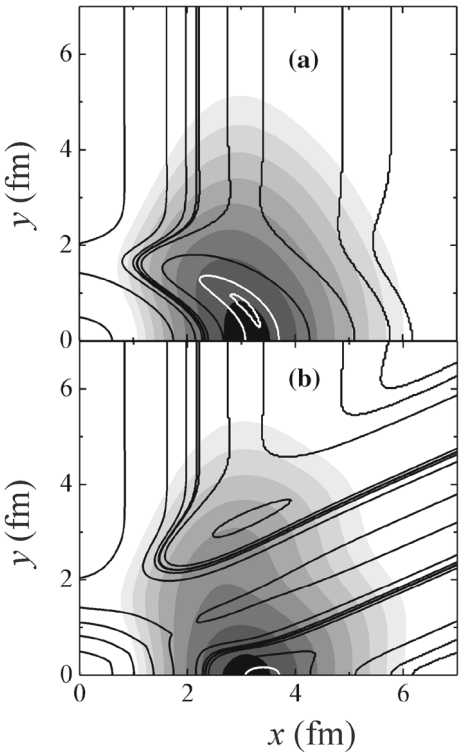

Fig. 17 The probability density (shades of grey; logarithmic scale) for the ground state of the ^{9}Be nucleus as a $2\alpha + n$ system along with the potential landscape (curves) in the case of the distances (83) $\mathbf{x} \perp \mathbf{y}$ (**a**) and $\mathbf{x} \parallel \mathbf{y}$ (**b**) calculated by the HSF method for DWS α-α potential (54), (55) together with α-neutron pseudopotentials (82) with parameters from Table 8 ($U_3 = 107.13$ MeV)

ground state energies and to study the spatial structures for the nuclei ^{10}Be, ^{10,11}B, ^{10,11}C.

5.3 Spatial structures of the nuclei ^{10}Be, ^{10}B, ^{10}C as 4-body systems

The experimental $E_{s,\mathrm{exp}}$ and calculated (using the FPI method) $E_{s,\mathrm{calc}} = -E_0$ values of energy of separation of the nuclei ^{10}Be, ^{10,11}B, ^{10,11}C into α-clusters, nucleons, and light nuclei are given in Table 10.

The results of calculations of the propagator $b_0{}^{-1} \ln \tilde{K}_{\mathrm{E}}$ are presented in Fig. 18. The distribution of the probability density for four-body configurations of ^{10}Be ($2\alpha + 2n$) was studied in [48,64]. The configuration $\alpha + 2n + \alpha$ with the closely located valence neutrons (dineutron cluster n^2) between α-clusters is the most probable. The dinuclear configuration α+^{6}He is less probable. For the ^{10}C nucleus ($\alpha + 2p + \alpha$ system), the physical distances proportional to the normalized Jacobi coordinates are similar to those for the ^{10}Be nucleus:

$$\begin{aligned} &\mathbf{x} = \mathbf{r}_{\alpha_2} - \mathbf{r}_{\alpha_1},\ \mathbf{y} = \mathbf{r}_{p_2} - \mathbf{r}_{p_1}, \\ &\mathbf{z} = \tfrac{1}{2}\left(\mathbf{r}_{p_1} + \mathbf{r}_{p_2}\right) - \tfrac{1}{2}\left(\mathbf{r}_{\alpha_2} + \mathbf{r}_{\alpha_1}\right). \end{aligned} \tag{86}$$

Table 10 The experimental $E_{s,\mathrm{exp}}$ and calculated $E_{s,\mathrm{calc}} = -E_0$ values of energy (MeV) of separation of nuclei into α-clusters, nucleons, and light nuclei

Nuclei	$E_{s,\mathrm{exp}}$	$E_{s,\mathrm{calc}}$	Method
^{10}Be ($2\alpha + 2n$)	8.380	8.48±0.12	FPI
^{10}B ($2\alpha + n + p$)	8.159	8.28±0.20	FPI
^{10}B (α+ ^{6}Li)	4.461	3.41±0.30	FPI
^{10}C ($2\alpha + 2p$)	3.728	2.67±0.15	FPI
^{10}C (α+ ^{6}Be)	−0.03	-0.2 ± 0.13	FPI
^{11}B ($2\alpha + 2n + p$)	19.613	19.34±0.80	FPI
^{11}C ($2\alpha + n + 2p$)	16.848	16.51±0.80	FPI

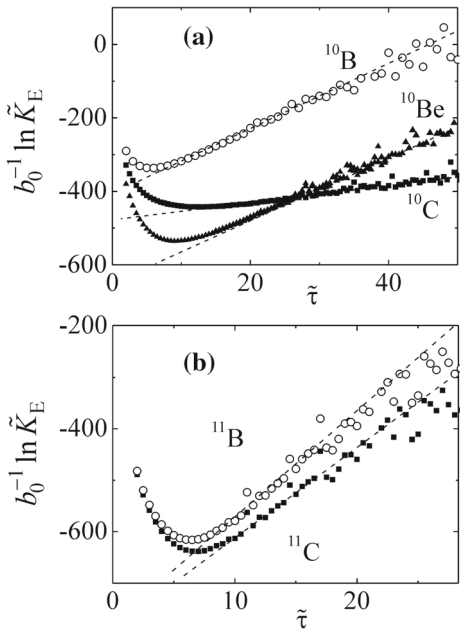

Fig. 18 Dependence of the normalized logarithm of the propagator $\tilde{K}_{\mathrm{E}}$ (23) on imaginary time τ for nuclei consisting of α-clusters and nucleons: (a) ^{10}Be ($2\alpha + 2n$), ^{10}B ($2\alpha + n + p$), ^{10}C ($2\alpha + 2p$); (b) ^{11}B ($2\alpha + 2n + p$), ^{11}C ($2\alpha + n + 2p$); (c) ^{12}C (3α), ^{16}O (4α). The straight lines are the results of linear regression applied to the linear intervals of the graphs

For the ^{10}B nucleus ($\alpha + p + n + \alpha$ system), the similar physical distances are

$$\begin{aligned} &\mathbf{x} = \mathbf{r}_{\alpha_2} - \mathbf{r}_{\alpha_1},\ \mathbf{y} = \mathbf{r}_{p} - \mathbf{r}_{n}, \\ &\mathbf{z} = \tfrac{1}{2}\left(\mathbf{r}_{p} + \mathbf{r}_{n}\right) - \tfrac{1}{2}\left(\mathbf{r}_{\alpha_2} + \mathbf{r}_{\alpha_1}\right), \end{aligned} \tag{87}$$

where the masses of protons and neutrons are considered to be equal. The triplet potential $V_t(r)$ was used to describe the interaction between a proton and a neutron in the ^{10}B nucleus.

Expression (20) is an explicit form of the square modulus of the coordinate wave function depending on the potential energy of the system. Therefore, calculations of the probability density using formula

$$|\Psi_0(\mathbf{x},\mathbf{y},\mathbf{z})|^2 \approx \tilde{K}_{\rm E}\,(\mathbf{x},\mathbf{y},\mathbf{z},\tau;\mathbf{x},\mathbf{y},\mathbf{z},0) \tag{88}$$

yield unnormalized coordinate wave function

$$\Psi_0(\mathbf{x},\mathbf{y},\mathbf{z}) \approx \sqrt{\tilde{K}_{\rm E}\,(\mathbf{x},\mathbf{y},\mathbf{z},\tau;\mathbf{x},\mathbf{y},\mathbf{z},0)} \tag{89}$$

which is symmetric with respect to permutation of α-clusters for the nuclei ^{10}B, ^{10}C. The coordinate wave function (89) is symmetric with respect to permutation of two protons with the total spin $S = 0$ for the ^{10}C nucleus.

The examples of the probability density distributions for four-body configurations of ^{10}C $(2\alpha + 2p)$ are shown in Fig. 19. The value of $K_{\rm E}$ is the combination (4) for the probability density $|\Psi_0(\mathbf{x},\mathbf{y},\mathbf{z})|^2$ of the ground state and $|\Psi_1(\mathbf{x},\mathbf{y},\mathbf{z})|^2$ for the first exited state of the system $(2\alpha+2p)$. Narrow maximum 1 of $\tilde{K}_{\rm E}$ in Fig. 19a and the most probable configuration 1 with valence protons (diproton cluster p^2) between α-clusters $(\alpha + p^2 + \alpha)$ correspond to the ground state of the ^{10}C nucleus. Regions 2 and 3 correspond to configurations 2 and 3 of the ground state with larger distances between particles in the system. Maxima 4 and 6 in Fig. 19b and configurations 4 and 6 may correspond to the first exited state with oscillatory relative motion of the α-cluster and ^{6}Be between the central repulsive core and the top of the Coulomb barrier. The ground state partially corresponds to broad maximum 4 in Fig. 19b.

The examples of the probability density distribution for four-body configurations of ^{10}B $(2\alpha + p + n)$ are shown in Fig. 20; they are similar to the distributions for ^{10}C $(2\alpha+2p)$. Narrow maximum 1 of $\tilde{K}_{\rm E}$ in Fig. 20a and the most probable configuration 1 with a valence neutron and proton (deuteron cluster d) between α-clusters $(\alpha + d + \alpha)$ correspond to the ground state of the ^{10}B nucleus. The spread of the probability density distribution for the ^{10}B nucleus is less than for the ^{10}C nucleus because the energy of its separation into α-clusters and nucleons is greater than that for ^{10}C.

The comparison of dependence of the propagator $\tilde{K}_{\rm E}\,(\mathbf{x},\mathbf{y},\mathbf{z},\tau;\mathbf{x},\mathbf{y},\mathbf{z},0)$ on $\tilde{\tau} = \tau/t_0$ near maxima for short and long distances between α-particles (clusters) in the nuclei ^{10}B and ^{10}C is shown in Fig. 21. The energies of excited states determined via linear regression on linear segments are given in Table 10. They are close to the experimental values of energies of nucleus separation: $^{10}\mathrm{B} \to {}^4\mathrm{He} + {}^6\mathrm{Li}$ and $^{10}\mathrm{C} \to {}^4\mathrm{He} + {}^6\mathrm{Be}$, respectively (see, e.g., [3]). The topography of the propagator $\tilde{K}_{\rm E}\,(x,y,z;\tilde{\tau})$ in Jacobi coordinates $\mathbf{x}\perp\mathbf{y}$, $\mathbf{z} \parallel \mathbf{x}$ for large distances between the centers of mass of α-particles and nucleons $z = 7$ fm shown in Fig. 22 allows us to find the probability densities $|\Psi_n|^2$ for individual excited states of the system $(2\alpha + p + n)$. The local maxima correspond to decay of the system into the deuteron and the ^{8}Be nucleus (configuration 1), ^{4}He and ^{6}Li nuclei (configurations 2 and 3). Extended region 4 corresponds to decay of the system into two ^{4}He nuclei and the deuteron.

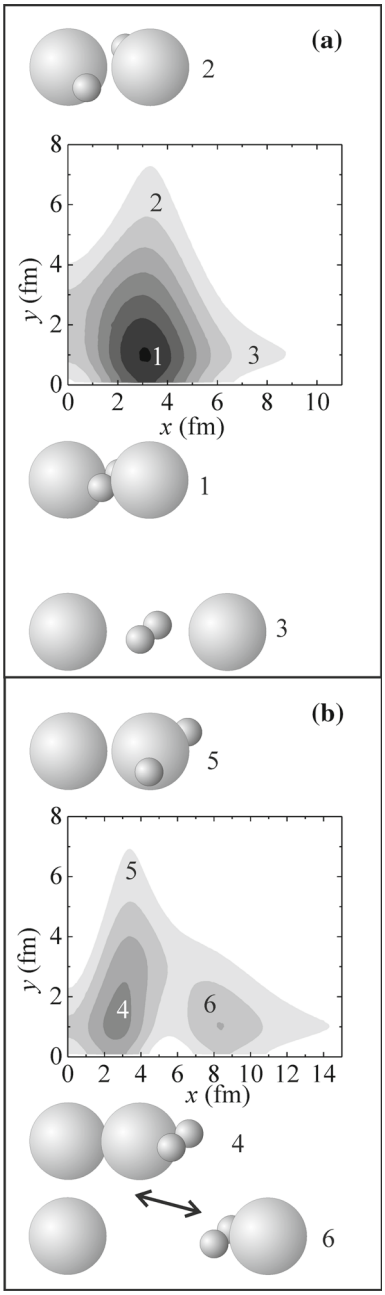

Fig. 19 Topography (logarithmic scale) of the propagator $\tilde{K}_{\rm E}$ (20) for the ^{10}C $(2\alpha+2p)$ nucleus at $\tau/t_0 = 12$ in the distances (86) $\mathbf{x}\perp\mathbf{y}$, $z = 0$ (a) and $\mathbf{x}\perp\mathbf{y}$, $\mathbf{z} \parallel \mathbf{x}$, z =2.5 fm (b) with the examples of the positions of protons (small spheres) and α-clusters (large spheres). Configuration 1 is the most probable and corresponds to the ground state; configurations 4 and 6 may correspond to the first exited state with oscillatory relative motion (along the arrow) of the α-cluster and the ^{6}Be nucleus between the central repulsive core and the top of the Coulomb barrier

5.4 Spatial structures of the nuclei ^{11}B, ^{11}C as 5-body systems

For the ^{11}B nucleus ($\alpha + 2n + p + \alpha$ system), the physical distances proportional to the normalized Jacobi coordinates are (see Fig. 23)

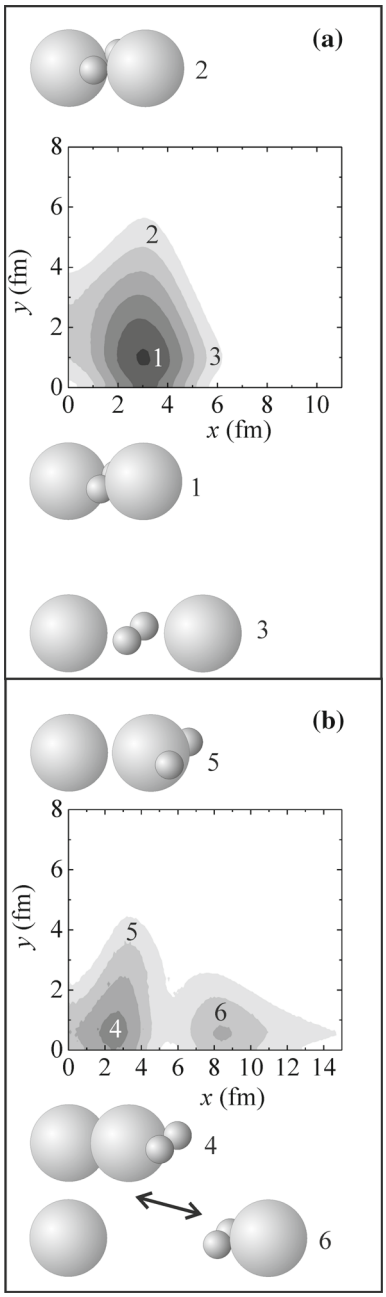

Fig. 20 Topography (logarithmic scale) of the propagator $\tilde{K}_{\rm E}$ (20) for the ^{10}B ($2\alpha+p+n$) nucleus at $\tau/t_0 = 12$ in the distances (87) $\mathbf{x}\perp\mathbf{y}$, $z = 0$ (a) and $\mathbf{x}\perp\mathbf{y}$, $\mathbf{z} \parallel \mathbf{x}$, $z = 2.5$ fm (b) with the examples of the positions of nucleons (small spheres) and α-clusters (large spheres). Configuration 1 is the most probable and corresponds to the ground state; configurations 4 and 6 may correspond to the first exited state with oscillatory relative motion (along the arrow) of the α-cluster and the ^{6}Li nucleus between the central repulsive core and the top of the Coulomb barrier

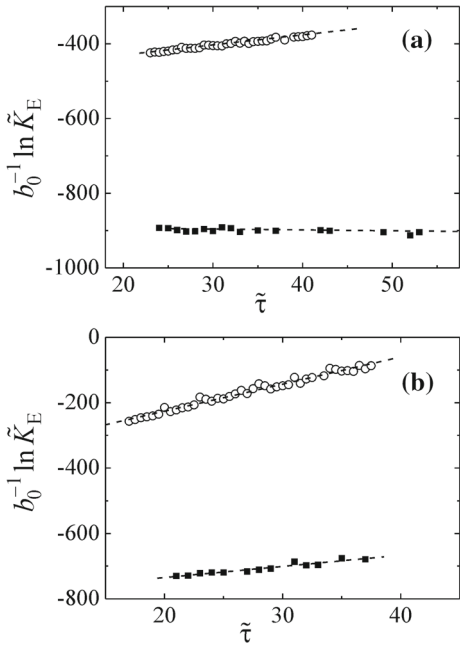

Fig. 21 The normalized logarithm of the propagator as a function of imaginary time for ^{10}C (a) and ^{10}B (b) in the vicinity of the maxima corresponding to the ground states 1 (circles) and to the excited states 6 (squares) in Figs. 19, 20. The lines are the result of linear regression applied to the linear parts of the plots

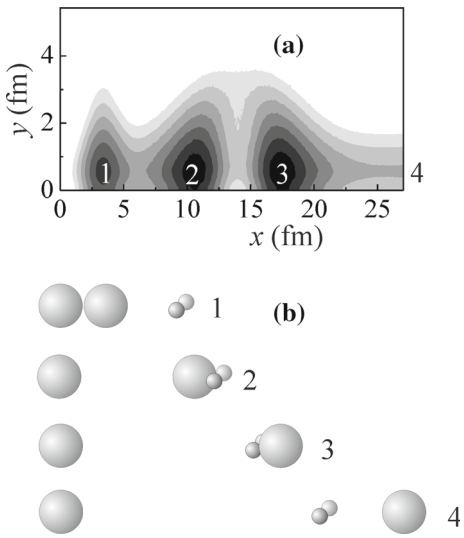

Fig. 22 Topography (logarithmic scale) of the propagator $\tilde{K}_{\rm E}$ (20) at $\tau/t_0 = 12$ in the distances (87) $\mathbf{x}\perp\mathbf{y}$, $\mathbf{z} \parallel \mathbf{x}$, $z = 7$ fm for **a** individual excited states of the system ($2\alpha+p+n$) with **b** examples of the positions of nucleons (small spheres) and α-particles (large spheres). Configuration 1 corresponds to separation of the system into the deuteron and the ^{8}Be nucleus; configurations 2 and 3 correspond to separation into ^{4}He and ^{6}Li nuclei; configuration 4 corresponds to separation into two ^{4}He nuclei and the deuteron

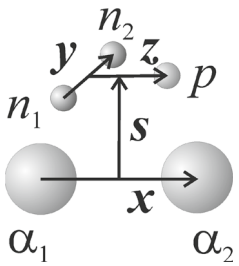

Fig. 23 The physical distances proportional to the normalized Jacobi coordinates (24), (25) for the ^{11}B nucleus ($\alpha+2n+p+\alpha$ system) along with the positions of nucleons (small spheres) and α-clusters (large spheres)

$$\begin{aligned}
&\mathbf{x} = \mathbf{r}_{\alpha_2} - \mathbf{r}_{\alpha_1},\ \mathbf{y} = \mathbf{r}_{n_2} - \mathbf{r}_{n_1},\\
&\mathbf{z} = \mathbf{r}_p - \tfrac{1}{2}\left(\mathbf{r}_{n_2} + \mathbf{r}_{n_1}\right),\\
&\mathbf{s} = \tfrac{1}{2}\left(\mathbf{r}_{n_1} + \mathbf{r}_{n_2} + \mathbf{r}_p\right) - \tfrac{1}{2}\left(\mathbf{r}_{\alpha_2} + \mathbf{r}_{\alpha_1}\right).
\end{aligned} \tag{90}$$

The potential energy for the ^{11}B nucleus

$$\begin{aligned}
V_{^{11}\mathrm{B}} = {} & V^{(\mathrm{N})}_{p,n,n} + V_{p-\alpha}(|\mathbf{r}_p - \mathbf{r}_{\alpha_1}|) + V_{p-\alpha}(|\mathbf{r}_p - \mathbf{r}_{\alpha_2}|)\\
& + V_{n-\alpha}(|\mathbf{r}_{n_1} - \mathbf{r}_{\alpha_1}|) + V_{n-\alpha}(|\mathbf{r}_{n_1} - \mathbf{r}_{\alpha_2}|)\\
& + V_{n-\alpha}(|\mathbf{r}_{n_2} - \mathbf{r}_{\alpha_1}|) + V_{n-\alpha}(|\mathbf{r}_{n_2} - \mathbf{r}_{\alpha_2}|)\\
& + V_{\alpha_2-\alpha_1}(|\mathbf{r}_{\alpha_2} - \mathbf{r}_{\alpha_1}|)
\end{aligned} \tag{91}$$

includes nucleon–nucleon part (80). The examples of the probability density distribution for five-body configurations of ^{11}B ($2\alpha+p+2n$) are shown in Fig. 24; they are similar to the distributions for ^{11}C ($2\alpha+n+2p$). Narrow maximum 1 of $\tilde{K}_{\mathrm{E}}$ in Fig. 24c and the most probable configuration 1 with valence neutrons and a proton (triton cluster t in the form of a regular triangle) between α-clusters ($\alpha+t+\alpha$) correspond to the ground state of the ^{11}B nucleus. Similar to the configuration of ^{11}B, a valence neutron and protons (^{3}He-cluster) between α-clusters ($\alpha+{}^3$He+α) correspond to the ground state of the ^{11}C nucleus.

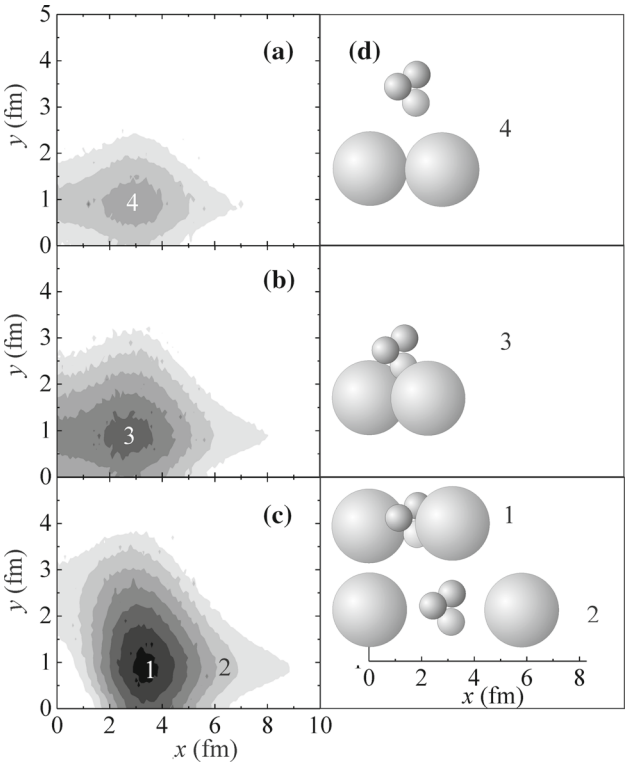

Fig. 24 Topography (logarithmic scale) of the propagator $\tilde{K}_{\mathrm{E}}$ (20), which is approximately equal to the probability density $|\Psi_0(\mathbf{x},\mathbf{y},\mathbf{z})|^2$ of the ground state of the ^{11}B ($2\alpha+p+2n$) nucleus, at τ/t_0 =10 for the distances (90) $\mathbf{x}\perp\mathbf{y}\perp\mathbf{z}$, $\mathbf{z}\parallel\mathbf{s}$, $z=y\sqrt{3}/2$, $s=3$ (**a**), s =2 fm (**b**), s =0 fm (**c**) with the examples of the positions of nucleons (small spheres) and α-clusters (large spheres) (**d**). Configuration 1 with valence neutrons and a proton (triton cluster t in the form of a regular triangle) between α-clusters ($\alpha+t+\alpha$) corresponds to the ground state of the ^{11}B nucleus; configurations 2, 3, and 4 are less probable

6 Conclusion

Calculations of the probability densities of the ground states for α-cluster nuclei ^{12}C(3α), ^{16}O (4α), ^{20}Ne (5α), ^{24}Mg (6α), ^{28}Si (7α) were performed by the Feynman Path Integral (FPI) method. The Hyperspherical Functions (HSF) method with cubic spline interpolation was used to calculate the ground state and the Hoyle state of the ^{12}C nucleus. It was shown that the structure of the Hoyle state corresponds to oscillations of α-clusters between the most probable compact regular triangle configuration and the linear dinuclear configuration near the top of the multi-dimensional Coulomb barrier. The spatial structures of the ground states of ^{12}C and ^{16}O correspond to simple geometric shapes, a regular triangle and a tetrahedron, respectively, with wide α-cluster clouds in their vertices. The ^{24}Mg nucleus has the shape of a pair of equal regular triangles with wide α-cluster clouds in their vertices as well. These results of the α-cluster model are similar to the results of the simple shell model of compact nuclei. The structures of the nuclei ^{10}Be, ^{10}B, ^{10}C, ^{11}B, ^{11}C were studied using the FPI method. These nuclei have molecular structure with valence neutrons and/or protons between two α-clusters. The used pairwise α-α, α-nucleon, and nucleon-nucleon potentials reproduced the experimental binding energies of N-body system rather than data on 2-body elastic scatterng.

It must be admitted that the FPI method has limited capabilities: it provides the possibility of calculating the energies and the probability densities only for the ground states of few-body systems. However, in some cases, the FPI method may be applied to studying the excited states with the distribution of the probability density not overlapping with that for the ground state. This method may be useful in the cases when the use of more exact methods is very laborious, particularly, for the systems with the number of particles more than four and for realistic potentials with repulsive cores.

Acknowledgements The author thanks the HybriLIT team for the technical support of parallel calculations on the Heterogeneous Cluster of the Joint Institute for Nuclear Research and Dr. M.A. Naumenko for assistance in the development of software for parallel calculations.

Data Availability Statement This manuscript has no associated data or the data will not be deposited. [Authors' comment: This is a theoretical study and no experimental data.]

A Simulating a random vector with the multidimensional Gaussian distribution

A standard algorithm for simulating a random vector Q distributed according to (12) consists in sequential generation of the values of its components from the conditional distributions $W_1(q_1|q_0), W_2(q_2|q_0, q_1), \ldots, W_{N-1}(q_{N-1}|q_0, q_1, q_2, \ldots, q_{N-2})$, where

$$W = W_k(q_k|q_0, q_1, q_2, \ldots, q_{k-1}) \tag{92}$$

is the probability density for the values of q_k for the given values of $q_0, q_1, q_2, \ldots, q_{k-1}$. The one-dimensional distribution for $k = 1$,

$$\begin{aligned} W_1(q_1|q_0) &= \int dq_2 \ldots \int dq_{N-1} W \\ &= \tfrac{1}{\sqrt{2\pi}\sigma_1} \exp\left\{-\tfrac{1}{2\sigma_1}\left[(q_1 - q_0)^2\right]\right\}, \end{aligned} \tag{93}$$

is a normal distribution with expectation

$$\mathrm{M}q_1 = q_0 \tag{94}$$

and variance

$$\sigma_1 = \frac{\Delta\tau\hbar}{m}\left(1 - \frac{1}{N}\right). \tag{95}$$

The two-dimensional distribution for $k = 2$ is the product of the normal distributions for q_1 and q_2,

$$\int dq_3 \ldots \int dq_{N-1} W = W_2(q_2|q_0, q_1)\, W_1(q_1|q_0), \tag{96}$$

where

$$W_2(q_2|q_0, q_1) = \frac{1}{\sqrt{2\pi}\sigma_2} \exp\left\{-\frac{1}{2\sigma_2}\left[(q_2 - \mathrm{M}q_2)^2\right]\right\}, \tag{97}$$

$$\mathrm{M}q_2 = \left(1 - \frac{1}{N-1}\right) q_1 + \frac{1}{N-1} q_0, \tag{98}$$

$$\sigma_2 = \frac{\Delta\tau\hbar}{m}\left(1 - \frac{1}{N-1}\right). \tag{99}$$

In general, the distribution $W_k(q_k|q_0, q_{k-1})$ is also a normal distribution with expectation

$$\mathrm{M}q_k = (1 - A_k)\, q_{k-1} + A_k q_0,\ A_k = \frac{1}{N-k+1} \tag{100}$$

and variance

$$\sigma_k = \frac{\Delta\tau\hbar}{m}(1 - A_k). \tag{101}$$

When simulating a trajectory, the next random value q_k is calculated by the formula:

$$q_k = \mathrm{M}q_k + \zeta_k \Delta q_k, k = \overline{1, N-1}, \tag{102}$$

where $\Delta q_k = \sqrt{\sigma_k}$ is the root-mean-square deviation and ζ_k is a normally distributed random variable with zero expectation and a unity variance.

References

1. K. Ikeda, N. Takigawa, H. Horiuchi, Prog. Theor. Phys. Suppl. **Extra No.**, 464 (1968)
2. H. Horiuchi, K. Ikeda, Y. Suzuki, Prog. Theor. Phys. Suppl. **52**, 89 (1972)
3. V.I. Zagrebaev, A.S. Denikin, A.V. Karpov, A.P. Alekseev, M.A. Naumenko, V.A. Rachkov, V.V. Samarin, V.V. Saiko, *NRV Web Knowledge Base on Low-Energy Nuclear Physics*, http://nrv.jinr.ru/
4. Y. Kanada-En'yo, H. Horiuchi, Prog. Theor. Phys. Suppl. **142**, 205 (2001)
5. H. Horiuchi, K. Ikeda, K. Kato, Prog. Theor. Phys. Suppl. **192**, 1 (2012)
6. W. Von Oertzen, M. Freer, Y. Kanada-En'yo, Phys. Rep. **432**, 43 (2006)
7. M. Freer, Rep. Prog. Phys. **70**, 2149 (2007)
8. Q. Zhao, Z. Ren, M. Lyu, H. Horiuchi, Y. Funaki, G. Röpke, P. Schuck, A. Tohsaki, C. Xu, T. Yamada, B. Zhou, Phys. Rev. C **97**, 054323 (2018)
9. Q. Zhao, Z. Ren, M. Lyu, H. Horiuchi, Y. Kanada-En'yo, Y. Funaki, G. Röpke, P. Schuck, A. Tohsaki, C. Xu, T. Yamada, B. Zhou, Phys. Rev. C **100**, 014306 (2019)
10. M. Lyu, Z. Ren, H. Horiuchi, B. Zhou, Y. Funaki, G. Röpke, P. Schuck, A. Tohsaki, C. Xu, T. Yamada, Eur. Phys. J. A **57**, 51 (2021)
11. W. von Oertzen, Nucl. Phys. A **148**, 529 (1970)
12. S. Okabe, Y. Abe, Prog. Theor. Phys. **61**, 1049 (1979)
13. D. Scharnweber, W. Greiner, U. Mosel, Nucl. Phys. A **164**, 257 (1971)
14. Chart of nucleus shape and size parameters. http://cdfe.sinp.msu.ru/services/radchart/radmain.html
15. P. Descouvemont, T. Druet, L.F. Canto, M.S. Hussein, Phys. Rev. C **91**, 024606 (2015)
16. S.M. Lukyanov, M.N. Harakeh, M.A. Naumenko, Yi Xu, W.H. Trzaska, V. Burjan, V. Kroha, J. Mrazek, V. Glagolev, Š. Piskoř, J. Nucl. Sci. Technol. World **5**, 265 (2015)
17. M.V. Zhukov, L.V. Chulkov, B.V. Danilin, A.A. Korsheninnikov, Nucl. Phys. A **533**, 428 (1991)
18. M.V. Zhukov, B.V. Danilin, D.V. Fedorov, J.M. Bang, I.J. Thompson, J.S. Vaagen, Phys. Rep. **231**, 151 (1993)
19. B.V. Danilin, I.J. Thompson, J.S. Vaagen, M.V. Zhukov, Nucl. Phys. A **632**, 383 (1998)
20. I.J. Thompson, B.V. Danilin, V.D. Efros, J.S. Vaagen, J.M. Bang, M.V. Zhukov, Phys. Rev. C **61**, 024318 (2000)
21. Yu. Ts. Oganessian, V.I. Zagrebaev, J.S. Vaagen, Phys. Rev. C **60**, 044605 (1999)
22. K.-I. Kubo, M. Hirata, Nucl. Phys. A **187**, 186 (1972)
23. J. Bang, C. Gignoux, Nucl. Phys. A **313**, 119 (1979)
24. V.I. Kukulin, V.M. Krasnopol'sky, V.T. Voronchev, P.B. Sazonov, Nucl. Phys. A **417**, 128 (1984)
25. A. Diaz-Torres, I.J. Thompson, C. Beck, Phys. Rev. C **68**, 044607 (2003)
26. C. Beck, N. Keeley, A. Diaz-Torres, Phys. Rev. C **75**, 054605 (2007)
27. R.P. Feynman, A.R. Hibbs, *Quantum Mechanics and Path Integrals* (McGraw-Hill, New York, 1965)
28. P. Descouvemont, C. Daniel, D. Baye, Phys. Rev. C **67**, 044309 (2003)
29. E.M. Tursunov, J. Phys. G Nucl. Part. Phys. **27**, 1381 (2001)

30. E.M. Tursunov, D. Baye, P. Descouvemont, Nucl. Phys. A **723**, 365 (2003)
31. V.I. Kukulin, V.M. Krasnopol'sky, M.A. Miselkhi, V.T. Voronchev, Sov. J. Nucl. Phys. **34**, 11 (1981)
32. E.M. Tursunov, K.D. Razikov, V.I. Kukulin, V.T. Voronchev, V.N. Pomerantsev, Phys. Atom. Nucl. **57**, 2075 (1994)
33. Y. Suzuki, M. Takahashi, Phys. Rev. C **65**, 064318 (2002)
34. M. Hesse, D. Baye, J. Phys. B **32**, 5605 (1999)
35. M. Hesse, Phys. Rev. E **65**, 046703 (2002)
36. H. Suno, Y. Suzuki, P. Descouvemont, Phys. Rev. C **91**, 014004 (2015)
37. H. Suno, Y. Suzuki, P. Descouvemont, Phys. Rev. C **94**, 054607 (2016)
38. D.V. Fedorov, A.S. Jensen, Phys. Lett. B **389**, 631 (1996)
39. A. Cobis, D.V. Fedorov, A.S. Jensen, Phys. Rev. Lett. **79**, 2411 (1997)
40. N. Barnea, M. Viviani, Phys. Rev. C **61**, 034003 (2001)
41. A. Tohsaki, H. Horiuchi, P. Schuck, G. Röpke, Phys. Rev. Lett. **87**, 192501 (2001)
42. Y. Kanada-En'yo, H. Horiuchi, A. Ono, Phys. Rev. C **52**, 628 (1995)
43. Y. Kanada-En'yo, H. Horiuchi, Phys. Rev. C **52**, 647 (1995)
44. N.K. Timofeyuk, Phys. Rev. C **78**, 054314 (2008)
45. A.A. Slavnov, L.D. Faddeev, *Gauge Fields: An Introduction to Quantum Theory* (Westview Press, Boulder, CO, 1993)
46. E.V. Shuryak, O.V. Zhirov, Nucl. Phys. B **242**, 393 (1984)
47. D.I. Blokhintsev, *Principles of Quantum Mechanics* (Allyn and Bacon, Boston, 1964)
48. V.V. Samarin, M.A. Naumenko, Phys. Atom. Nucl. **80**, 877 (2017)
49. M.A. Naumenko, V.V. Samarin, Supercomp. Front. Innov. **3**, 80 (2016)
50. NVIDIA CUDA, http://developer.nvidia.com/cuda-zone/
51. J. Sanders, E. Kandrot, *CUDA by Example: An Introduction to General-Purpose GPU Programming* (Addison-Wesley, New York, 2011)
52. Heterogeneous Cluster, Joint Institute for Nuclear Research, http://hybrilit.jinr.ru/
53. G.I. Marchuk, *Methods of Numerical Mathematics* (Springer-Verlag, New York, 1982)
54. V.V. Samarin, M.A. Naumenko, IL Nuovo Cimento **42C**, 130 (2019)
55. S. Ali, A.R. Bodmer, Nucl. Phys. **80**, 99 (1966)
56. V.V. Samarin, J. Phys. Conf. Ser. **1555**, 012030 (2020)
57. V.V. Samarin, Bull. Russ. Acad. Sci. Phys. **76**, 866 (2012)
58. W.J. Vermeer, M.T. Esat, J.A. Kuehner, R.H. Spear, A.M. Baxter, S. Hinds, Phys. Lett. B **122**, 23 (1983)
59. V.I. Zagrebaev, V.V. Samarin, Phys. Atom. Nucl. **67**, 1462 (2004)
60. V.V. Samarin, Phys. Atom. Nucl. **78**, 128 (2015)
61. I.R. Afnan, Y.C. Tang, Phys. Rev. **175**, 1337 (1968)
62. R.A. Arndt, R.H. Hackman, L.D. Roper, Phys. Rev. C **15**, 1002 (1977)
63. V.V. Samarin, M.A. Naumenko, Bull. Russ. Acad. Sci. Phys. **83**, 411 (2019)
64. V.V. Samarin, Bull. Russ. Acad. Sci. Phys. **84**, 981 (2020)
65. G. Erens, J.L. Visschers, R. van Wageningen, Ann. Phys. (NY) **67**, 461 (1971)
66. T.K. Das, H.T. Coelho, M. Fabre de la Ripelle, Phys. Rev. C **26**, 2281 (1982)
67. W. Oehm, S.A. Sofianos, H. Fiedeldey, M. Fabre de la Ripelle, Phys. Rev. C **42**, 2322 (1990)
68. H. Kanada, T. Kaneko, S. Nagata, M. Nomoto, Prog. Theor. Phys. **61**, 1327 (1979)
69. W.A. Harrison, *Pseudopotentials in the Theory of Metals* (W.A. Benjamin, New York, 1966)